D1.6 – Report on optical diagnostics for fuel films, mixture inhomogeneities, soot and water injection in optical engines. Focus is on implications for models for design and control.
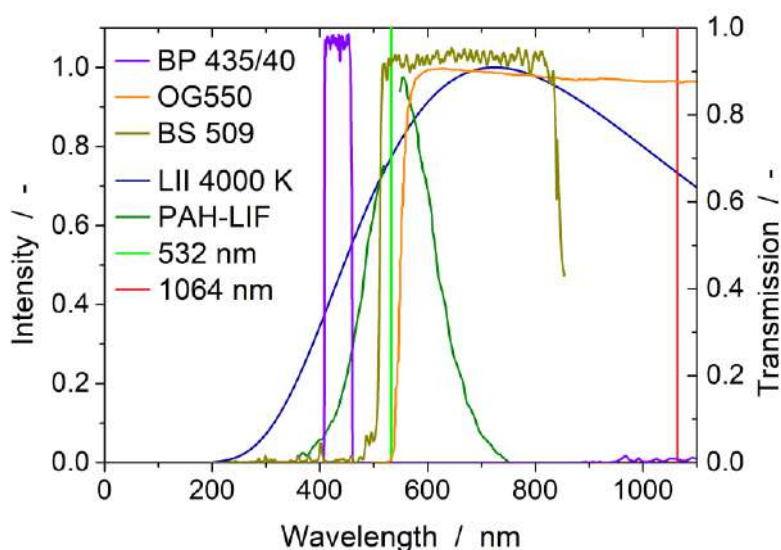
PaREGEn

bandpass filters BP 435/40 and OG550. The latter captured the red-shifted part of the PAH LIF. The BP 435/40 was used to capture soot LII and to avoid the interference of C_2 and C_3 emissions, induced by strong laser irradiance of soot.

Figure 18 Blackbody radiation at 4000 K (LII signal), PAH LIF excited at 532 nm in a laminar diffusion flame [24], excitation wavelengths, and transmission of beam splitter and bandpass filters used for simultaneous PAH LIF and soot LII.

Figure 19 shows the mean LII signal from a central and an annular region of interest (ROI) in the flame of the Santoro burner for varying laser fluences. 100 images were captured for each laser fluence. The central ROI is indicated in the LII image in the bottom right of Figure 19. The annular ROI was dynamically chosen in each image around the particular maximum LII signal in the right flank of the flame. Also shown is the result from Bladh *et al.* who modelled the LII signal (thermal radiation) of soot, excited by a Gaussian laser sheet at 1064 nm, for different laser fluences and captured with a 18 ns gate, starting 20 ns after the pulse. The LII signal was calculated from a model, describing the heat- and mass-transfer between soot and the gaseous environment, and by assuming a certain polydisperse particle-size distribution. For small laser fluences the temperature of the soot particles increases linearly with the laser fluence such that, according to the Stefan-Boltzmann law, the LII signal increases proportionally to T^4. At a certain fluence, some particles reach the sublimation temperature of soot (about 4000 K). Therefore, a further increase in the laser fluence does not contribute to a further heating of those particles but to vaporization, indicating the turning point of the function. Then, solely particles that have not reached the sublimation temperature contribute to an increase in the LII signal with increasing laser fluence. At a certain fluence, all particles reach the sublimation temperature such that the LII signal does not increase anymore with increasing laser fluence [44]. This plateau region is much more pronounced when exciting with a Gaussian sheet instead of a top-hat profile. In the former case, the signal loss due sublimation of soot particles in the high-fluence centre of the Gaussian sheet is compensated for by the increasing signal in the low fluence wings. This plateau regime is highly desired in LII imaging of relative soot concentrations since then a higher signal intensity can exclusively be attributed to a higher concentration of soot. The result from this work shows a saturation of the LII signal at a laser fluence of about 0.5 J/cm².

According to the findings from Santoro *et al.*, soot particles in the annular region of the flame are larger than particles in the centre region at higher heights above the nozzle (HAB). The explanation is that strong nucleation and growth occur at low HAB in the annular region of the flame whilst more moderate nucleation rates occur in the central region at higher HAB [45]. Since soot particles in the central region of the flame are expected to be on average smaller than the particles in the annular region, they are also expected to be heated to a higher temperature for the same laser fluence due to a higher specific surface area. However, the normalized LII signal detected in the central region is lower than the one from the right annular

D1.6 – Report on optical diagnostics for fuel films, mixture inhomogeneities,
soot and water injection in optical engines. Focus is on implications for models for design and control.

PaREGEn

region (ROI right) up to a fluence of 0.5 J/cm². Also, in contrast to the fluence curve from the right ROI, it seems that the curve in the central ROI does not saturate throughout the investigated fluence range. The reason for that is that younger soot has a lower absorption function such that it is heated to the sublimation temperature at higher laser fluence than more mature soot [46].

With these findings the laser fluence for LII imaging was chosen to 0.5 J/cm². The laser fluence for imaging of PAH LIF was chosen to 0.008 J/cm² to avoid the interference with LII signal.
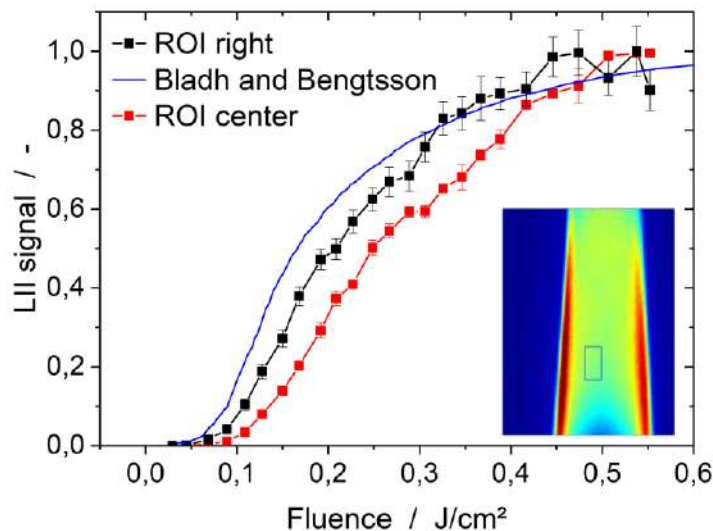

Figure 19: LII signal versus laser fluence from two regions of interest and from Bladh et al. [47].

Figure 20 shows ensemble average images of 1500 single shots of PAH LIF (left) at a laser fluence of 0.008 J/cm² and of 1500 single shots of soot LII (centre) at a laser fluence of 0.5 J/cm². Comparing the two images, shows soot LII, excited by the 532 nm laser sheet, also in the PAH LIF image. This is indicated by the minimum in the signal intensity in the PAH LIF image between the central and the annular region at a HAB of around 35 mm, which is between a layer of large PAH and soot. The soot LII image shows very high signal levels in the annular region from HAB 35 to 60 mm.
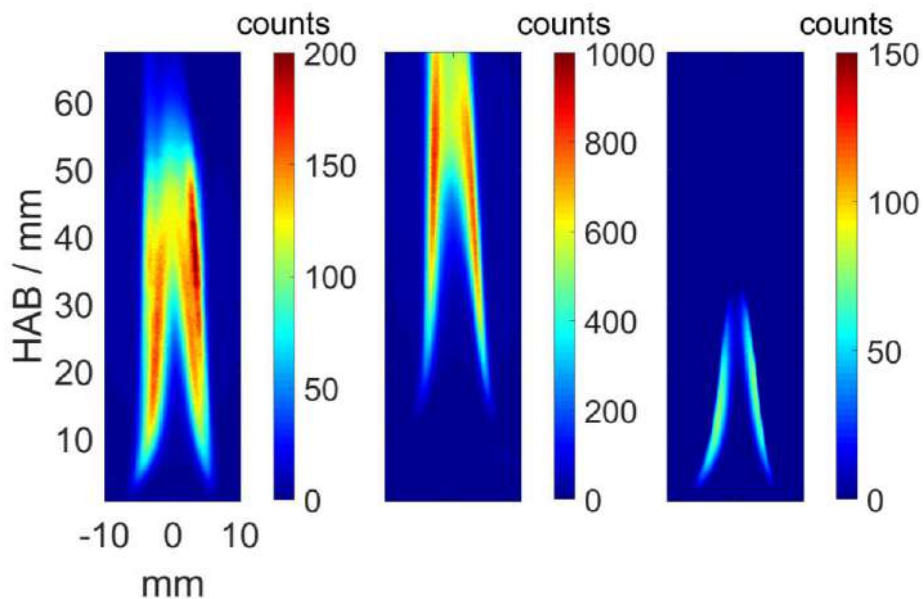

Figure 20: Ensemble average images of 1500 single shots of (left) PAH LIF and (centre) soot LII. (Right) Soot LII subtracted from PAH LIF.

In contrast to the LIF image, the LII image does not show signal in the hollow cone region near the fuel nozzle, indicating the presence of large PAH in that region. The dark region below the visualized PAH region is where the transition of fuel to small PAH is taking place. The edges of the PAH LIF cone are covered by regions of high soot LII signal, indicating the nucleation region where soot forms from PAH. The image on the right is the result of the subtraction of the LII image from the PAH image so that PAH is shown exclusively.

Images from simultaneous imaging of PAH LIF and soot LII are shown in Figure 21. The left hand side shows an ensemble average image of 1000 simultaneous single shots. The right hand side shows one single shot. Both images visualize large PAH in a hollow cone region near the fuel nozzle and soot in an annular region, surrounding the PAH cone, and above. The ensemble average shows the two signals more blurred compared to the single shot, stemming from flickering of the flame throughout the 1000 single shots.
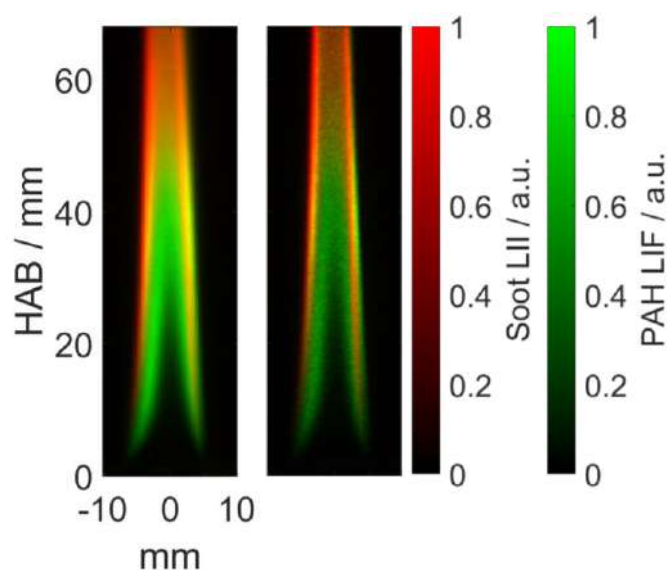

Figure 21: Simultaneous images of PAH LIF and soot LII. (Left) Ensemble average image of 1000 single shots and (right) single shot.

Figure 22 shows the PAH LIF and soot LII signals along the centreline with increasing HAB in the laminar diffusion flame of the Santoro burner.
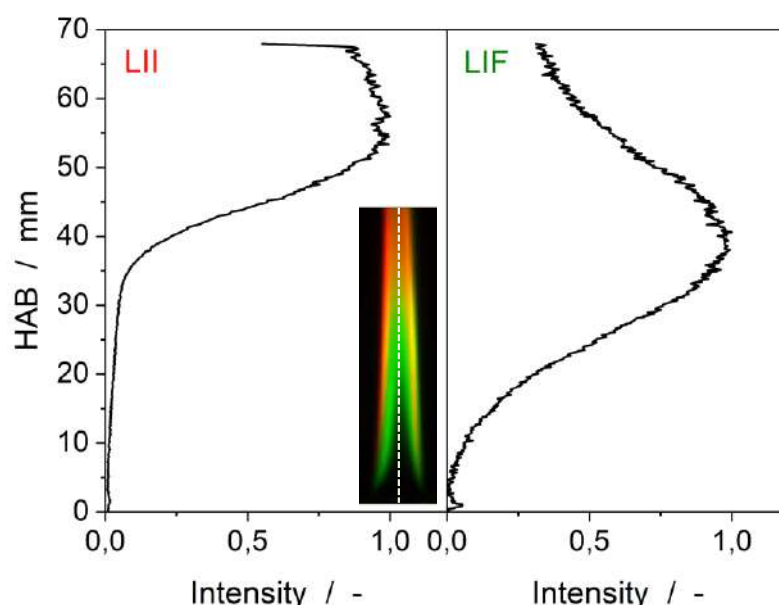

Figure 22: LII and LIF signals along the centreline with increasing HAB.

The LII signal starts to increase significantly at a HAB of about 30 mm and peaks at about 50 mm. The slight decrease in the LII signal is attributed to a decreasing temperature of soot particles and decreasing laser fluence towards the wing of the Gaussian sheet. Surprisingly, the LIF signal peaks at around 40 mm, in a region where the LII signal starts to significantly increase. This indicates that the nucleation rate of soot becomes larger than the formation rate of large PAH.

2.3.6   Diagnostic for water injection

In WP3 (i.e., outside of the scope of this deliverable, but in this project) FEV performed engine tests injecting water directly into the cylinder or into the intake port, while the VKA performed corresponding CFD simulations. To investigate the causes for the effects seen in these experiments and to validate the results of the simulations, spatially resolved measurements of where and how much water is on the walls and in the bulk gas of the combustion chamber are needed. Developing an optical technique for this purpose, to be applied in the optically accessible engine at BOSCH, is part of WP1.

Experiments reported in D1.5 already have shown the principal feasibility of detecting films of liquid water adhering to optically transparent walls -also curved ones, like in an optically accessible engine- via imaging of absorption of infrared (IR) light. Experiments at the IVG (outside of this project, not reported here in detail) show that for water films thicker than 10 μm, as expected in the current application, illumination and detection at around 1.4 μm wavelength is suitable. This is important because, in this wavelength band, mature and inexpensive diode lasers from the telecom industry are readily available. Cameras sensitive in this band are available at both IVG and BOSCH. Tuning of the diode current tunes the laser wavelength on or off the sharp absorption features of gaseous water and thereby allows distinguishing between liquid and gaseous water. Therefore, the technological building blocks for the proposed diagnostic technique are in place. However, in a deviation from the grant agreement, imaging experiments in the optical engine, proving the actual suitability of the diagnostic in the context of the project, were not performed in the period covered by this report. Instead, priority was given to the more complex than anticipated development of the diagnostics for fuel films, soot, and soot precursors (described above), because the knowledge gap in the area of in-cylinder soot formation from fuel films was considered more important.

Experiments on IR imaging in the optical engine at BOSCH and if necessary, in the flow channel at the IVG are planned for Q3 2019.

D1.6 – Report on optical diagnostics for fuel films, mixture inhomogeneities,
soot and water injection in optical engines. Focus is on implications for models for design and control.

PaREGEn

3 Implications for models for design and control

Results from fuel-film, combustion, soot, and soot precursor imaging are shown in this chapter. The results are mainly used in Task 1.4 by ETH for validation of simulations. Results from fuel-film imaging were already successfully reproduced in a CFD simulation by ETH. Currently, a CFD simulation on combustion, and the formation of PAH and soot near the evaporating fuel films, is set up by ETH. Results on quantitative fuel-film imaging in an optical engine have already been presented in Deliverable 1.2 and can be found in [1].

3.1 Fuel films

Figure 23 shows the thickness of the four optically accessible fuel films (1, 2, 4, and 5) 3 ms after start of injection as an ensemble average of 50 single injections. Fuel films 3 and 6 adhere to the metal frame around the quartz wall. In the origin of the image is the injector tip. The spray forming fuel film 1 collides with the spark electrodes so that the quantity of fuel reaching the wall is smaller than for fuel film 2. Note that the spray hitting the electrode is due to the off-design injector orientation here in the wind tunnel. In an actual engine, the spark plug would be between jets 1 and 2. Because of the longer spray cone penetration through the wind tunnel, this fuel-film is on average thinner than the ones in the bottom (films 4 and 5).
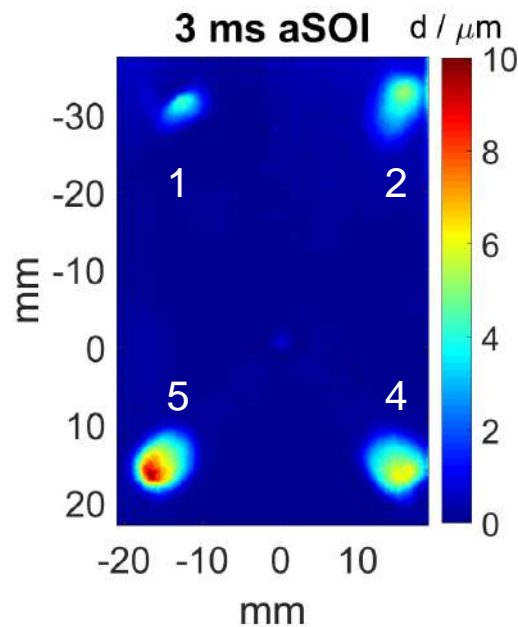

Figure 23: Fuel films on the quartz window 3 ms after start of injection.

Figures 24 and 25 show the temporal evolution of ensemble averages and single shots of the evaporating film 5 with combustion, i.e. after the fuel/air mixture has been ignited by the electrodes in the test section. The images in Figure 24 are ensemble averages of 50 single shots. In this case, the wall temperature is 352 K in this case, the injection duration is 0.5 ms (5 mg), and the flow velocity 1.8 m/s. For jets 1 and 2, the impingement angle (the angle between the spray cone axis and the wall) is approximately 50°. For jets 4 and 5 the impingement angle becomes approximately 70°. The orthogonal distance from the injector nozzle to the wall is about 32.5 mm.

The distance of the four fuel films from the injector nozzle, the origin of the image, is about 15 mm along the x-axis. Along the y-axis, it is about 15 mm for films 4 and 5 and 30 mm for films 1 and 2. Thus, the impingement distance along the spray axis is 39 mm for films 4 and 5 and 47 mm for films 1 and 2. The momentum of the spray cone in the vertical direction results in an accumulation of fuel in the outer part of the wetted area. Previous studies also found that the fuel film is thin in the spray impact area and accumulates toward the film tip [1, 48, 49]. Combustion of the fuel/air mixture is initiated 0.65 ms after end of injection. The

D1.6 – Report on optical diagnostics for fuel films, mixture inhomogeneities, soot and water injection in optical engines. Focus is on implications for models for design and control.

PaREGEn

propagation of the turbulent flame front through the mixture happens between 3 and 15 ms aSOI. Both the film's area and thickness decrease in time due to evaporation. The single shots show that fuel accumulates in small regions during evaporation, leading to the formation of discrete fuel "blobs" or droplets. Also Schulz *et al.* observed the contraction of the fuel film in some regions into such small, thick droplets [50]. The fuel film has almost completely evaporated at 75 ms aSOI.
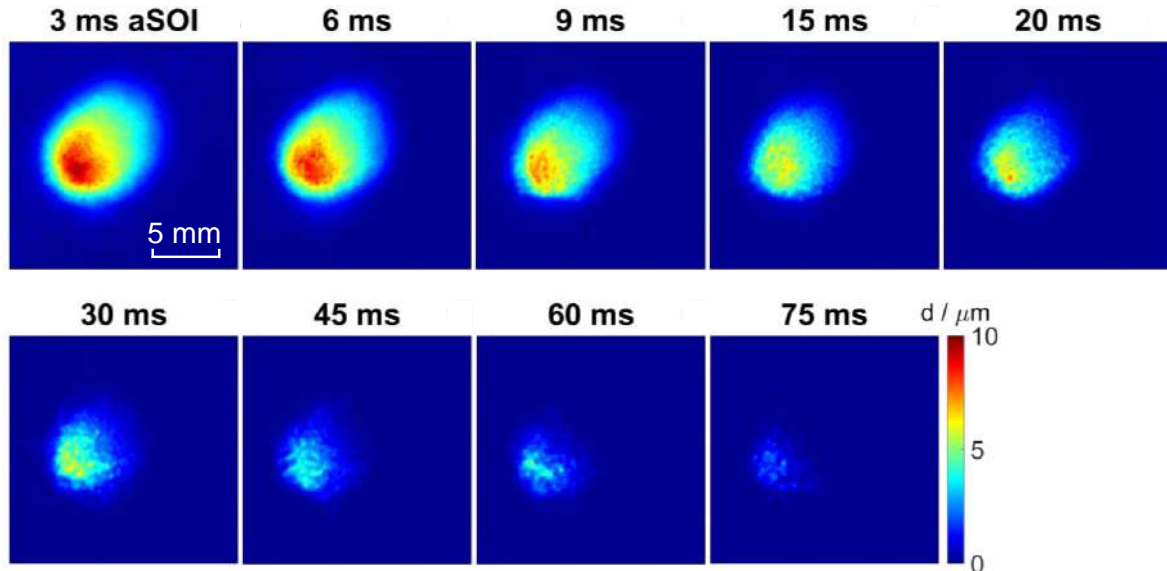

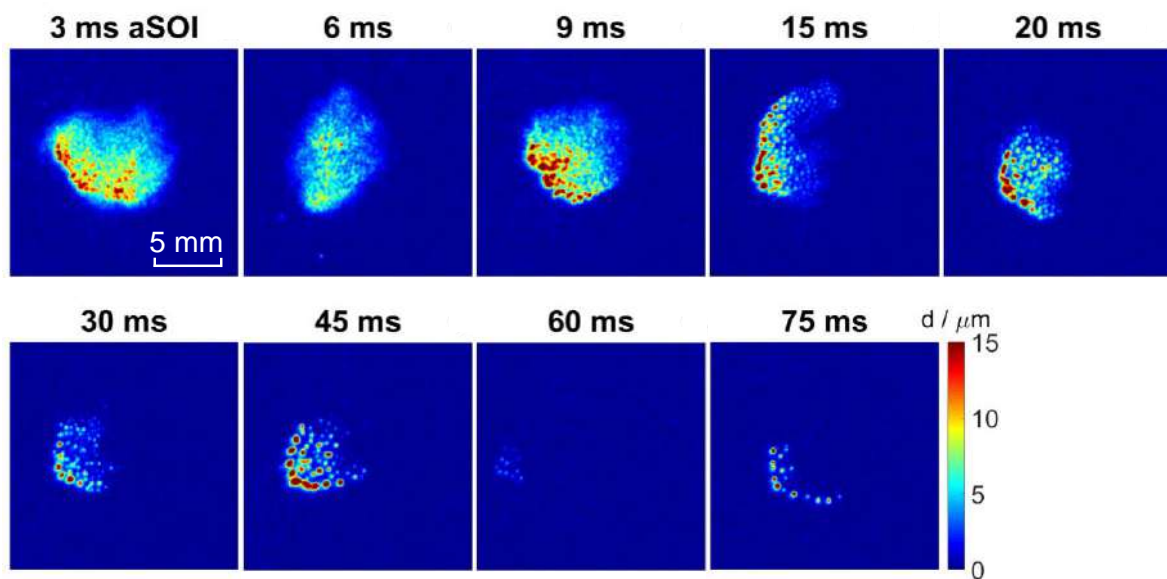Figure 24: Film evaporation: Ensemble average images of the thickness of film 5.

Figure 25: Film evaporation: Single shots of the thickness of film 5.

For the calculation of the total film area and volume the thickness images were analysed with a threshold at 1.5 μm film thickness. Multiplication of the film thickness with the projected pixel size and integration over the threshold area results in the total film volume. Multiplying the result with the density of iso-octane of 0.69 mg/mm³ yields the fuel-film mass. Figure 26 shows the decreasing mass and area of the four fuel films for the aforementioned conditions. Assuming that the total injected fuel mass of 5 mg splits evenly onto the six single spray cones, each spray cone contains 0.83 mg. Thus, about 20% of the injected fuel adheres to the wall in the bottom left area, forming film 5 (impingement angle 70°, impingement distance 39 mm, 100 bar fuel pressure). This is consistent with the results of Senda *et al.*, who found the adhering fuel fraction of iso-

D1.6 – Report on optical diagnostics for fuel films, mixture inhomogeneities, soot and water injection in optical engines. Focus is on implications for models for design and control.

PaREGEn

octane to be about 21% at ambient conditions for an impingement distance of 50 mm, an impingement angle of 65°, and an injection pressure of 300 bar [39]. For film 2 (impingement angle 50°, impingement distance 47 mm), only 15% of the injected mass adheres to the wall. Since in some images fuel film 4 is not captured completely and due to a slightly lower mean thickness, its initial mass is not equal to the one of fuel film 5. However, the evaporation rates are very similar. In general, the highest evaporation rates are early aSOI. The high evaporation rate in the beginning might come from fast mass transfer between the fuel film and the surrounding gas phase due to strong turbulence after injection. While the fuel accumulates to thick droplets in the outer part of the fuel film and remains until the end of evaporation, the thin parts of the film where the jet impinges on the wall evaporate first. For all films the area shrinks much more from 3 to 9 ms aSOI than within the following time intervals.
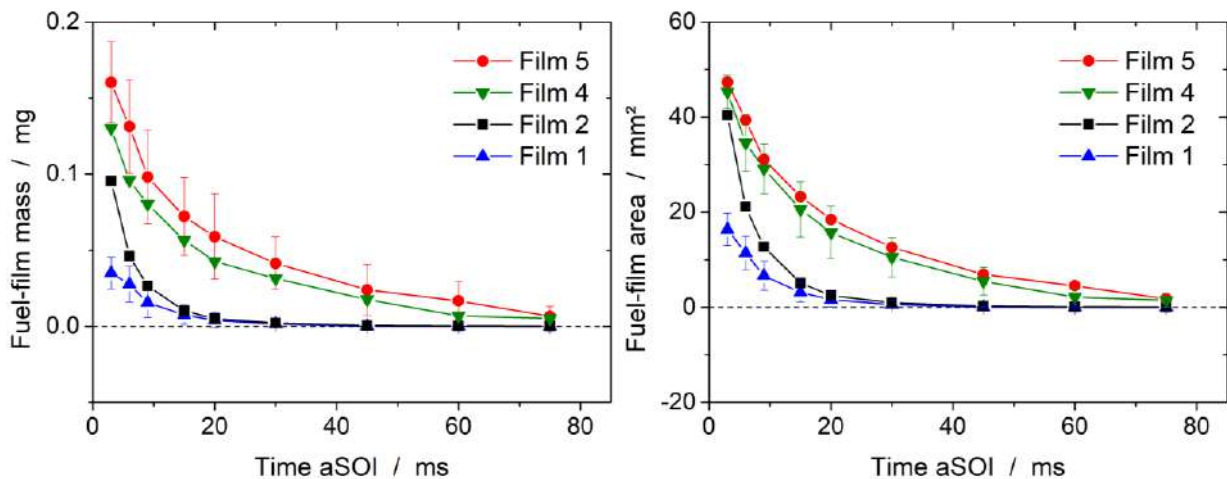

Figure 26: (left) Mass and (right) area of fuel films 1, 2, 4, and 5 during evaporation. Error bars indicate the standard deviation from 50 individual injections.

The following discussion on the influence of different operating parameters will focus on a comparison between film 2, also representing film 1, and film 5, also representing film 4.

The film area in Figure 26 shows that the initial area of films 5 and 2 are very similar. Senda *et al.* found qualitatively the same trend. The area remained constant for different impingement distances and angles, while the mean film thickness decreased for an increasing impingement distance and decreasing impingement angle [39]. Also, for low-pressure injection, Cheng *et al.* found the film area at 3 ms aSOI to be only slightly dependent on the impingement distance. They found that with an injection pressure of 3 bar and an impingement angle of 90°, the film area was 150 and 135 mm² for 50 and 60 mm distance, respectively [51]. Figure 27 additionally shows the temporal evolution of film 2.
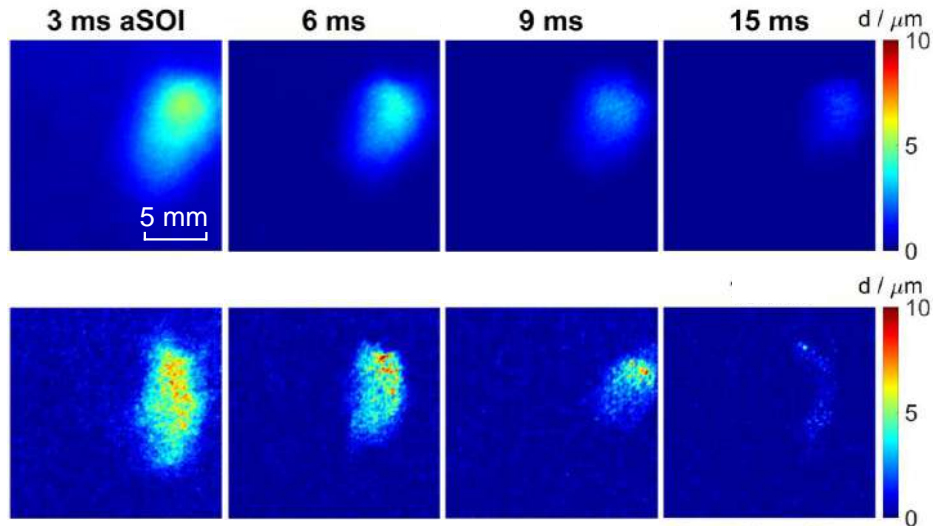
Figure 27: Film evaporation: (top) Ensemble average images of the thickness of film 2. (bottom) single shots of the thickness of film 2.

Since the initial areas of the two imaged fuel films (2 and 5) are similar (40 and 47 mm²) and the boundary conditions for conductive heat transfer from the wall to the liquid are similar, one might expect that similar fractions of the two films have evaporated at 10 ms aSOI. But from Figure 26 it is apparent that from film 5 0.03 and from film 2 0.05 mg evaporate in the first time interval. The explanation is that film 2 is 20% thinner than film 4, causing a lower heat capacity at 3 ms aSOI. Thus, evaporative cooling lowers the temperature of film 2 more than of film 5. As a consequence, the conductive heat flux from the wall increases due to the increasing temperature gradient, compensating for the evaporative cooling. As a result, a more of film 2 has evaporated at 6 ms aSOI than of film 5. Also, the concentration of fuel in the gas phase might be lower in the periphery of fuel films 1 and 2 since air flows from top to bottom such that films 4 and 5 are covered in, fuel/air mixture, transported downstream, inhibiting convective mass transfer. Additionally, the turbulent kinetic energy might also be higher in the top region than in the bottom. But it should be noted that also precision is poorer for film 2 due to the high quantity of thin regions.

Surprisingly, Figure 29 shows that the evaporation of both fuel films, 2 and 5, is not significantly affected by combustion. This implies that in our experiment convective heat transfer from the surrounding gas is negligible compared to the conductive heat transfer from the wall. This might be explained by the low heat transfer coefficient, about 11 W/(m²·K), between the gas phase and the liquid film.
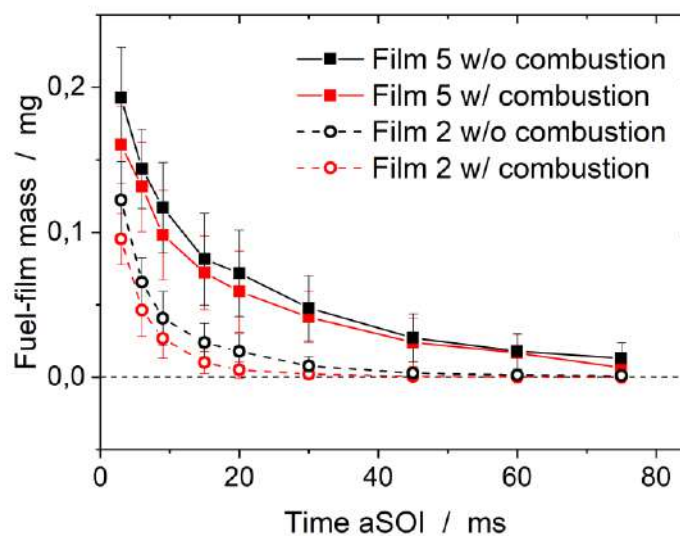
Figure 28: Mass of fuel films 2 and 5 with and without combustion during evaporation. Error bars indicate the standard deviation from 50 individual injections.

At 3 ms aSOI, film 5 has a mass of 0.16 mg with and 0.19 mg without combustion. The evaporation rate is about 60% higher for the case without combustion from 3 to 6 ms aSOI while the evaporation rate is similar at later times aSOI. Film 2 has an initial mass of 0.09 and 0.12 mg with and without combustion, respectively. Here, the evaporation rate is only 12% higher within the first time interval for the case without combustion. From high-speed imaging, Section 3.3, it is known that the flame front does not reach fuel film 5 in every combustion event for the injection duration of 0.5 ms. However, film 2 is reached by the flame front in every event and even here no significant influence is visible.

Figure 29 shows single shots of film 5 with and without combustion at 45 ms aSOI for an injection duration of 1 ms (9.3 mg). For this injection duration, the flame front reaches film 5 in almost every combustion event. In contrast to the aforementioned, the combustion significantly influences the evaporation between 30 and 45 ms aSOI. Again, the case with combustion shows a lower initial mass, about 14%, than the case without combustion. However, the evaporation rates are very similar from 3 to 30 ms aSOI. Beyond that time, the evaporation rate of the case with combustion is twice that high as the one for the case without combustion of 0.06 mg/ms. This effect might be explained by the diffusion flame reaching the fuel film, increasing the concentration gradient between the surface of the fuel film and its surrounding by consuming the fuel thereby increasing the mass transport.

D1.6 – Report on optical diagnostics for fuel films, mixture inhomogeneities, soot and water injection in optical engines. Focus is on implications for models for design and control.
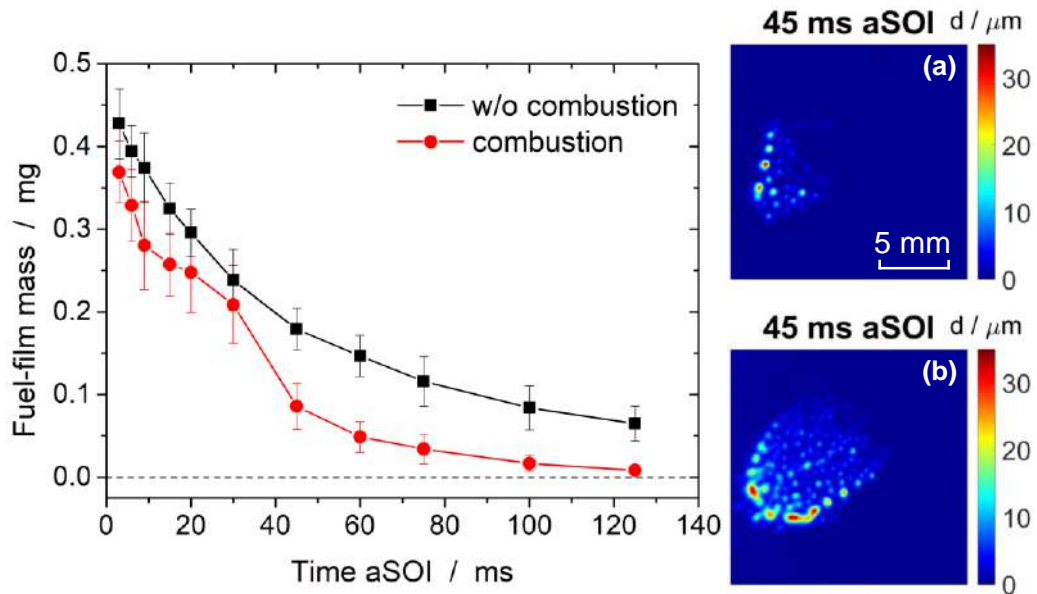
PaREGEn

Figure 29: (left) Mass of fuel film 5 with and without combustion during evaporation for 1 ms injection duration (10 mg). Error bars indicate the standard deviation from 50 individual injections. (right) Single shots of the thickness of film 5 (a) with combustion and (b) without combustion.

Beyond 45 ms aSOI the evaporation rates become similar again between the two cases. The images of the fuel films on the right hand side in Figure 23 show that the flame in particular causes the thin regions of the film, where the spray impinges, to evaporate quickly. Figure 30 compares the area and the thickness for the two cases. The systematic shift of the case with combustion to lower fuel-film masses is also represented by the fuel film area. However, the effect of the flame front reaching the fuel film at 30 ms aSOI seems to affect both the fuel-film area and thickness as both sharply decrease from 30 to 45 ms aSOI. The area decreases about a factor of six to finally 15 mm² without combustion while it has decreased almost to zero with combustion at 125 ms aSOI. In contrast to that, the mean fuel-film thickness does not change that much during evaporation. It decreases from 7.2 to 5.2 μm and from 7.2 to 6.3 μm with and without combustion, respectively.
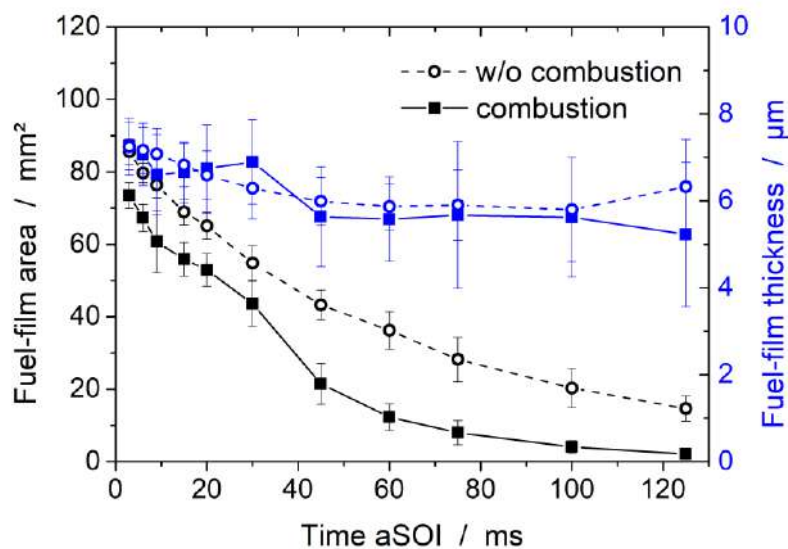

Figure 30: Area and thickness of fuel film 5 during evaporation with and without combustion. Error bars indicate the standard deviation from 50 individual injections.

Increasing the flow velocity in particular changes the initial mass of the fuel films, as shown in Figure 31. The film mass is about four times lower at 3 ms aSOI when increasing the flow velocity from 1.8 to 10 m/s. Surprisingly, an increase in the flow velocity from 6.5 to 10 m/s does not influence the evaporation of the film. The evaporation rates between 3 and 6 ms aSOI are about 0.014 mg/ms and 0.029 mg/ms for the cases with 1.8 and 6.5 m/s, respectively. However, also the film area is 57% lower at 3 ms aSOI when using a flow velocity of 6.5 instead of 1.8 m/s, explaining the 52% lower total evaporation rate. To investigate exclusively the influence of the flow velocity on the evaporation rate, the evaporation rate needs to be independent of the fuel-film area. Therefore, the absolute evaporation rate between two time steps aSOI was calculated, and normalized by the average fuel-film area between the two time steps. By that the evaporation rate becomes independent of the particular fuel-film area so that it only correlates with the parameter of interest. The right hand side of Figure 31 shows the area-normalized evaporation rate for the different flow velocities. In general, the evaporation rate is defined as:

$$\dot{m}_{Evap} = A \cdot \beta \cdot (\rho_{Sat} - \rho_\infty) \tag{8}$$

Here, A is the fuel-film area, β the mass transfer coefficient, and $(\rho_{Sat} - \rho_\infty)$ the mass-concentration gradient of fuel at the surface of the fuel-film and in the bulk of the gas flow. Therefore, a change in the area-normalized evaporation rate either signifies a change in the mass transfer coefficient or in the mass-concentration of fuel in the bulk gas, when assuming that the fuel-film temperature is equal. The right hand side of Figure 31 shows that the evaporation rates are similar at around 5 ms aSOI, where the high turbulence from the injection dominates the evaporation rate. Beyond 20 ms aSOI, the evaporation rates for the cases with 6.5 and 10 m/s exceed the ones from the cases with 1.8 and 3 m/s. First, the higher flow velocities result in an increase of the mass transfer coefficient β. Second, it also leads to a faster transport of gaseous fuel downstream such that the concentration gradient remains larger compared to the cases with lower flow velocity. Surprisingly, increasing the flow velocity from 6.5 to 10 m/s does not result in a higher evaporation rate. It needs to be taken into account that the calculated evaporation rate suffers from a poor precision. In particular, for the cases with 6.5 and 10 m/s, measured fuel-film thicknesses are thin, resulting in high precision uncertainty for the calculated evaporation rate.
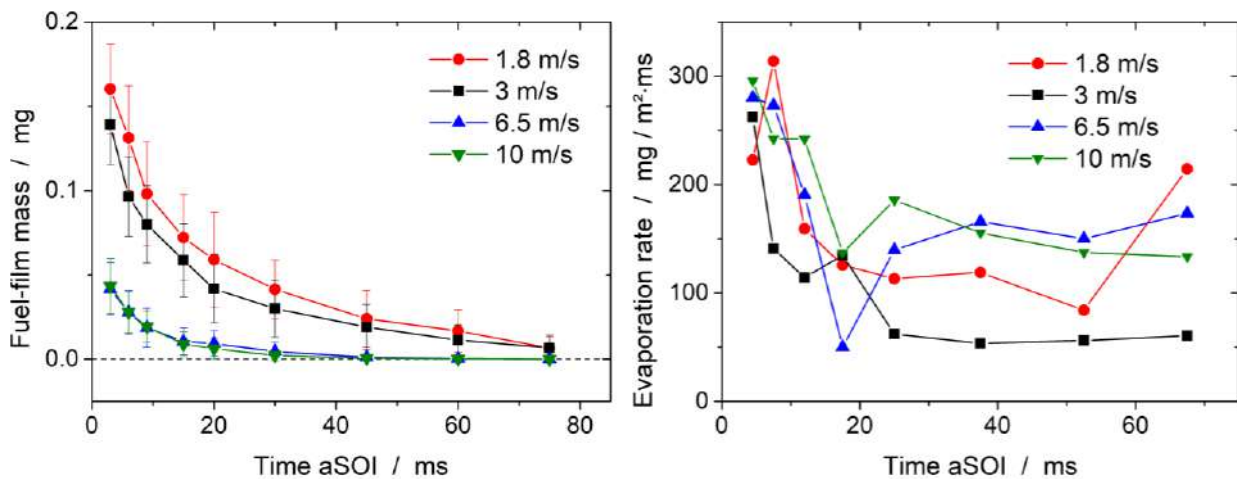

Figure 31: (left) Mass of fuel film 5 with and without combustion during evaporation for different air flow velocities. Error bars indicate the standard deviation from 50 individual injections. (right) Area normalized evaporation rate

Figure 34 shows the area and thickness of film 5 for the flow velocities 3 and 10 m/s. Apparently, the initial film area is more affected by the increasing flow velocity than the initial film thickness. While the area decreases about 57% from 47 to 20 mm² when increasing the flow from 1.8 to 10 m/s, the film thickness decreases only about 40%. Also, the film thickness remains approximately constant for the cases with 1.8 and 3 m/s and decreases from 2.9 to 0.4 µm for the cases with 6.5 and 10 m/s.

D1.6 – Report on optical diagnostics for fuel films, mixture inhomogeneities,
soot and water injection in optical engines. Focus is on implications for models for design and control.
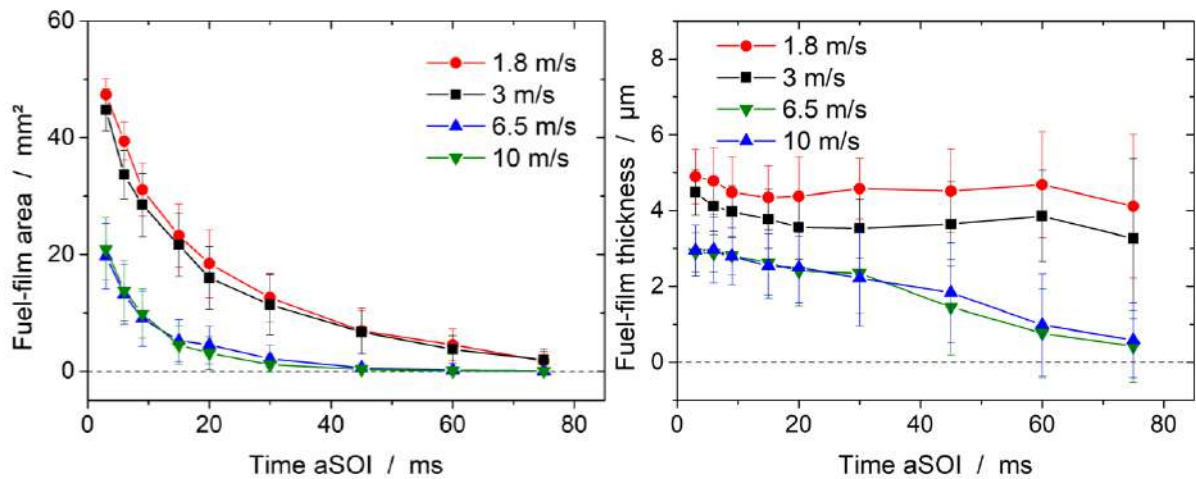
PaREGEn

Figure 32: (left) Area and (right) thickness of fuel film 5 during evaporation for different flow velocities. Error bars indicate the standard deviation from 50 individual injections.

Figure 33 shows single shots of fuel film 5 for the flow velocities 3 and 10 m/s. The images reveal that the formation of droplets seems to be more pronounced for lower flow velocities. For the flow velocities of 6.5 and 10 m/s the fuel accumulates to on average thicker blobs. Note that the scales are different between the two cases.
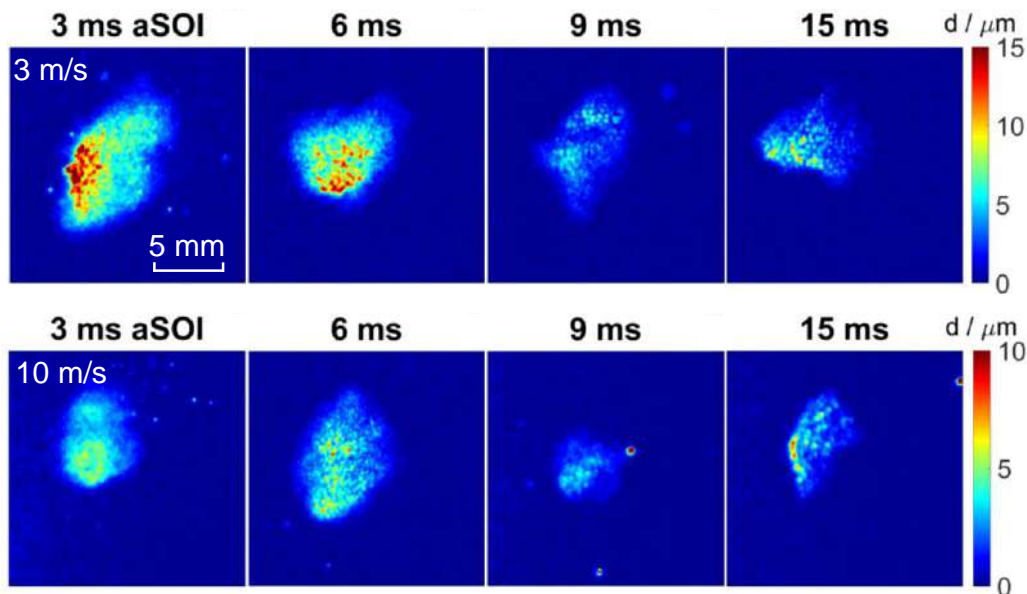

Figure 33: Film evaporation: Single shots of the thickness of film 5 for the flow velocities 3 and 10 m/s.

Figure 34 compares the fuel-film masses and evaporation rates over time aSOI for different injected masses. The initial mass of film 5 increases from 0.09 to 0.16 and to finally 0.37 mg for the injected masses of 3.3, 4.9, and 9.3 mg (0.3, 0.5 and 1 ms), respectively. The corresponding fractions of fuel adhering to the wall are 16%, 20% and 24%. The high injected mass comes along with a long injection duration so that late spray propagates through a fuel/air-mixture with a higher fuel-air ratio than early spray. This leads, according to Equation (8), to a smaller evaporation rate of the fuel droplets, and thus to larger fractions of fuel adhering to the wall. The area-normalized evaporation rates are similar between 3 and 9 ms aSOI. At later times aSOI the evaporation rate decreases for the injection masses 3.3 and 5 mg while it first decreases and then strongly increases from 30 to 45 ms aSOI for the case with 9.3 mg injection mass.

D1.6 – Report on optical diagnostics for fuel films, mixture inhomogeneities, soot and water injection in optical engines. Focus is on implications for models for design and control.
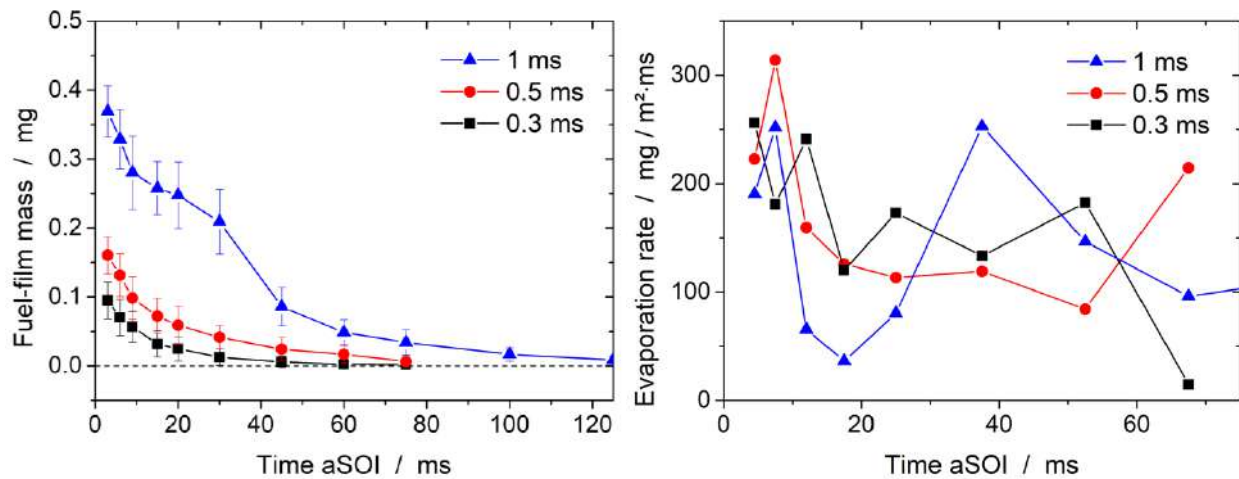
PaREGEn

Figure 34: Mass of fuel film 5 during evaporation for different injection durations. Error bars indicate the standard deviation from 50 individual injections. (right) Single shots.

Additionally, Figure 35 compares the mean fuel-film thickness and area for the three injection durations. The initial film area (3 ms aSOI) increases about 55%, while the film thickness increases about 48% for an injection mass of 9.3 mg, compared to an injection mass of 5 mg. The 55 % higher area mostly accounts for the 45% higher evaporation rate in the beginning. This also shows that the higher mean thickness does not significantly inhibit the evaporation early aSOI. Senda *et al.* found the mean film thickness to be constant at 20 μm when increasing the injection duration from 4 to 8 ms (increasing the injected mass of one spray cone from 7 to 14 mg). At the same time the area increased about 60% when injecting 50% more fuel [39]. This trend changes for very thin films. Maligne *et al.* investigated fuel films with thicknesses smaller than 1 μm and observed that the film thickness increases about 67% when increasing the injected mass by 50% [12]. Apparently, the results shown here are in the transition zone between the two aforementioned regimes since fuel-film area and thickness increase about the same magnitude. The injected mass of one spray cone is increased from 0.83 to 1.55 mg while the fuel films show thicknesses in the range of 5 μm.
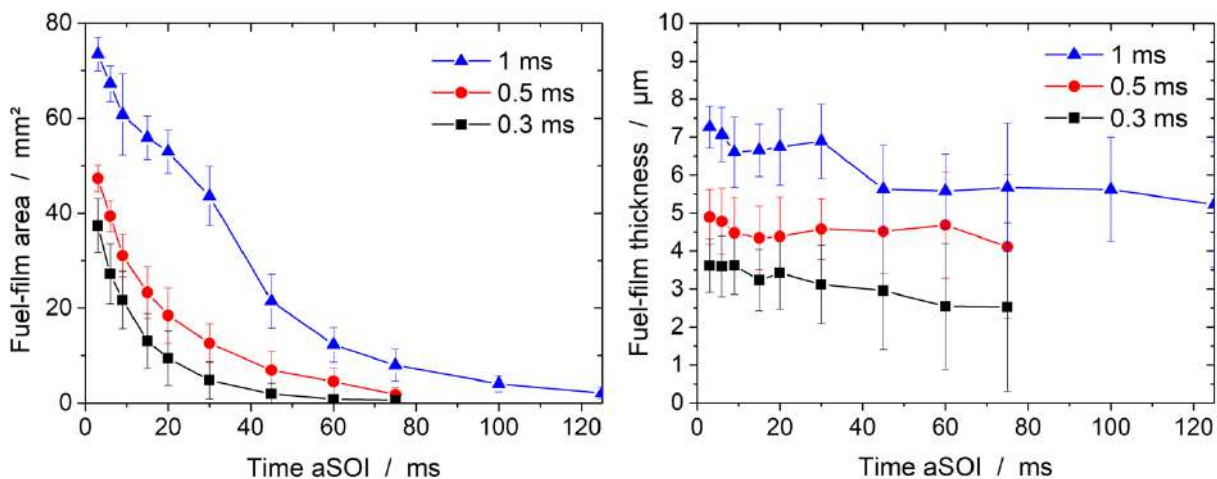

Figure 35: (left) Area and (right) thickness of fuel film 5 during evaporation for different injected masses. Error bars indicate the standard deviation from 50 individual injections.

Figure 35 also shows that during most of the evaporation the mean film thickness remains approximately constant for all injection durations. The sharp decrease in the covered area from 3 to 6 ms aSOI corresponds to the complete evaporation of the thin parts seen in the images in Figure 36. While the film looks blurry at the boundary 3 ms aSOI, it exhibits a sharp boundary at 6 ms aSOI. The decreasing area and the formation of

D1.6 – Report on optical diagnostics for fuel films, mixture inhomogeneities,
soot and water injection in optical engines. Focus is on implications for models for design and control.

PaREGEn

thick droplets, according to Figure 30, do not change much in the average film thickness (Figure 35), despite ongoing evaporation from the entire film.
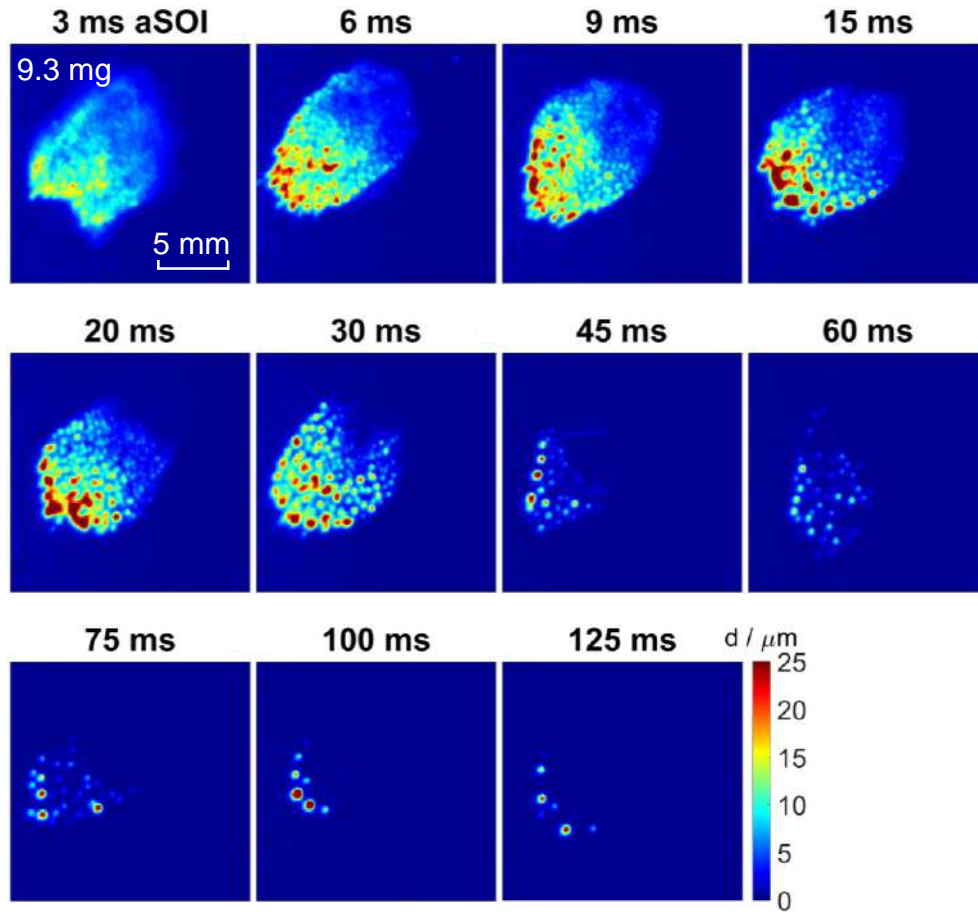

Figure 36: Film evaporation: Single shots of the thickness of film 5 for an injection mass of 9.3 mg.

Figure 37 shows the influence of the wall temperature on the evaporation rate of film 5. It should be taken into account that a lower wall temperature also leads to a lower air and also injector temperature. The liquid-fuel temperature before start of injection can be approximated by the injector temperature, which is about 8 K above the wall temperature. Thus, a higher wall temperature comes along also with a lower initial fuel-film mass since more fuel evaporates from the spray into the preheated air flow. The investigated wall temperatures are 332, 342 and 352 K. The corresponding air temperatures are 340, 361 and 381 K. The injection duration was 0.5 ms (5 mg). Figure 37 shows that the fuel-film mass adhering to the wall at 3 ms aSOI dramatically decreases with increasing temperature. The initial fuel-film masses are 0.38, 0.27 and 0.16 mg for the temperatures 332, 342 and 352 K. The right hand side of Figure 37 shows the area-normalized evaporation rates of film 5 for the different wall temperatures. Again, from 3 to 9 ms aSOI, the evaporation rates are expected to be governed by the strong convective mass transfer induced by the turbulent flow after the end of injection. During this time, a lower wall temperature, and hence film temperature and vapour pressure, do not affect the evaporation rate. After that, the curves on the right hand side in Figure 37 indicate an approximately constant evaporation rate From a model being currently developed in our group, it is known that the fuel film temperatures adapt to the wall temperature a few milliseconds after the end of injection. Therefore, an increase in the wall temperature results in an increase in the fuel-film temperature, which increases the fuel film's vapour pressure and thus also the saturation concentration of fuel ρ_{Sat} at the film surface. The latter results, according to Equation (8), in an increased evaporation rate. The film has almost completely evaporated at about 75 ms for a wall temperature of 352 K.

D1.6 – Report on optical diagnostics for fuel films, mixture inhomogeneities,
soot and water injection in optical engines. Focus is on implications for models for design and control.
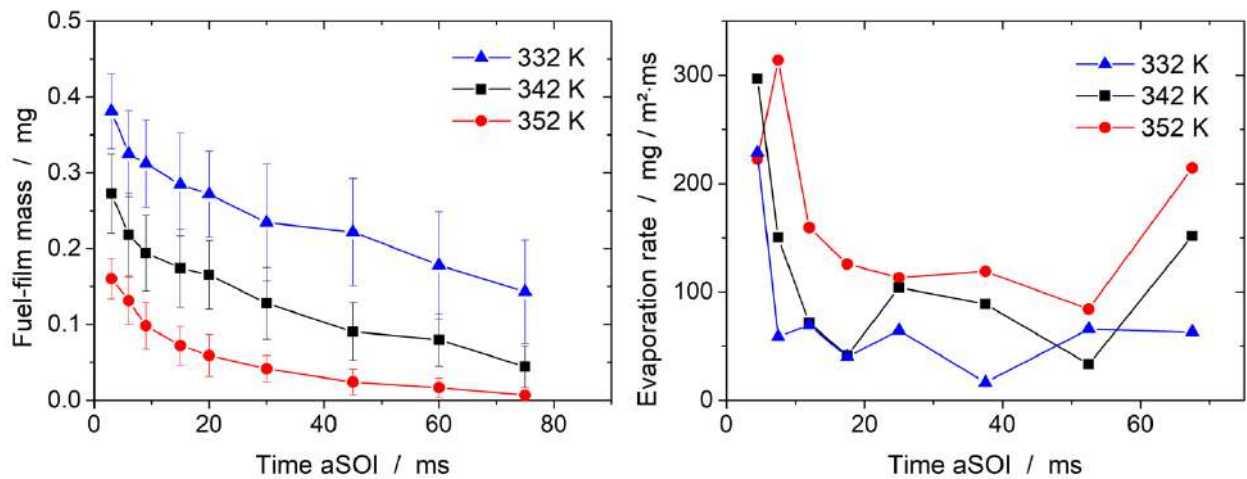
PaREGEn

Figure 37: Film 1 during evaporation for different quartz-wall temperatures, error bars indicate the standard deviation from 30 (at 3, 25, 75 and 100 ms aSOI) and 70 (at 10 and 50 ms aSOI) individual injections.

The fuel-film area and thickness to the different wall temperatures are shown in Figure 38. Again, the fuel-film thickness remains approximately constant. The area decreases strongest from 3 to 6 ms aSOI and linearly decreases beyond that time.
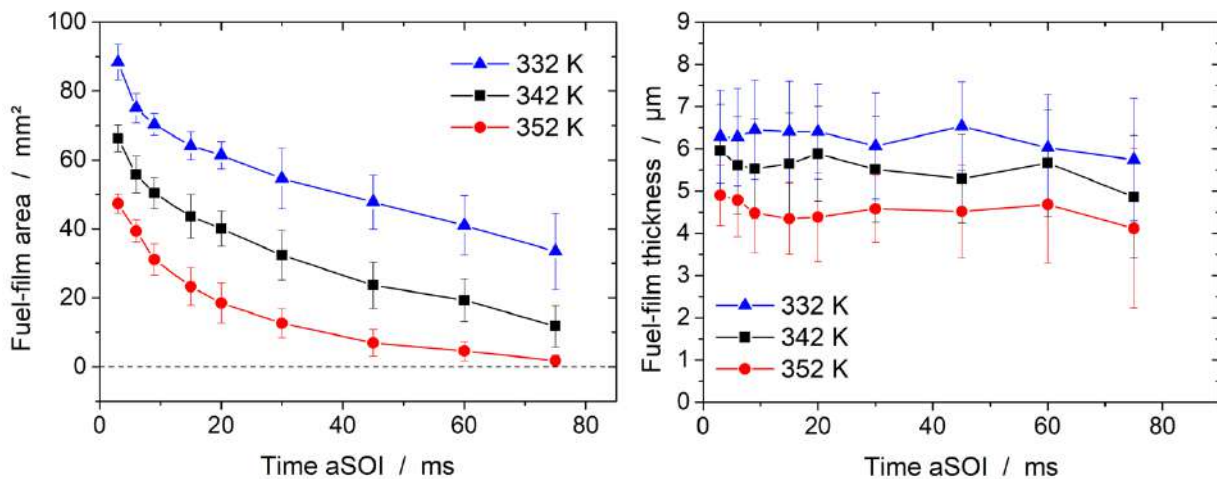

Figure 38: (left) Area and (right) thickness of fuel film 5 during evaporation for different injected masses. Error bars indicate the standard deviation from 50 individual injections.

Figure 39 shows single shots of the thickness of film 5 for the wall temperatures of 342 and 332 K. It is evident that both the fuel-film area and thickness are larger for a lower wall temperature. The images show that for a temperature of 342 K, the formation of thick fuel droplets is enhanced compared to the case with a temperature of 332 K. Apparently, the decreasing viscosity and the increasing diffusion coefficient of the liquid fuel with increasing temperature accelerate the accumulation of fuel to thick regions. As a conclusion, it seems that the wall temperature is the parameter that has the strongest influence on the evaporation rate of the fuel film. According to the images in Figure 39, even at 75 ms aSOI more than 50% of the initial film mass is present of film 5 for a wall temperature of 332 K.
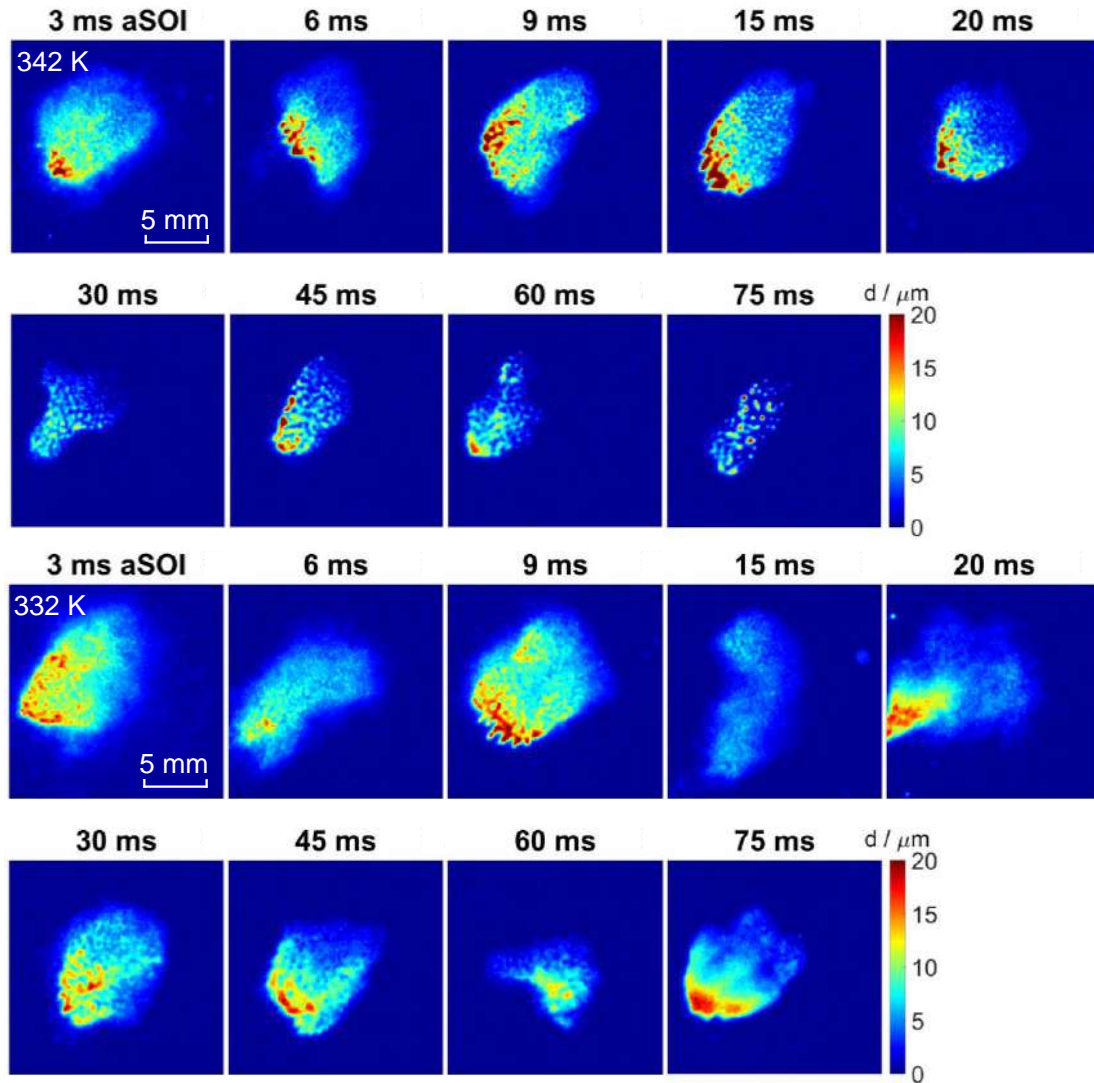
D1.6 – Report on optical diagnostics for fuel films, mixture inhomogeneities, soot and water injection in optical engines. Focus is on implications for models for design and control.

PaREGEn

Figure 39: Film evaporation: Single shots of the thickness of film 5 for wall temperatures 342 and 332 K.

3.2 Fuel vapour and combustion

The results presented in this section were done with an injector other than the project injector and under experimental conditions different from those shown in Table 1. An overview of the operating conditions and the optical layouts of the experiments with this injector setup can be found in [52].

Figure 40 shows images of the fuel-vapour distribution in the test section, visualized by LIF (top) and schlieren (bottom). Each LIF image is an ensemble average of 10 single shots. Note that measured mole fractions above 0.08 might be overestimated compared to actual mole fractions due deviations from the linear relation between the LIF signal and the fuel-vapour mole-fraction. The electrodes and the injector tip are schematically drawn in the top left image. The red dashed line in the second LIF image indicates the field of view for the schlieren imaging. The quartz window that the spray cones impinge on is on the right of the image. Fuel films 1 and 4 are centred at heights of about -20 and 35 mm, respectively, as indicated in the LIF image at 50 ms aSOI. The fuel-rich zone near the electrodes seen at 10 ms aSOI originates from the four spray cones that form fuel films 2, 3, 5, and 6. At 25 ms aSOI that zone mostly has been carried out of the light-sheet plane or downstream by the air flow. The detected fuel-vapour emerges mainly from films 1 and 4. Schlieren imaging visualizes the density gradients from fuel/air mixing integrated along the line of sight. At 10 ms aSOI the entire field of view is covered by such gradients, indicating the presence of fuel. Also in the schlieren images, the centre of film 1 is at a height of about -20 mm. The Schlieren images also show that

most of the vapour has already been carried out of the field of view (downwards) at 25 ms aSOI. Now the strongest gradients appear close to film 1, indicating its evaporation. At 50 ms aSOI film 4 has almost completely evaporated such that fuel-vapour fluorescence is almost exclusively detected near film 1. The corresponding schlieren image shows the convective transport of the vapour downstream along the wall. The LIF image at 100 ms aSOI shows that film 4 has completely evaporated while fuel still evaporates from the remaining film 1. Also, the schlieren image at 100 ms aSOI visualizes the evaporation of film 1.
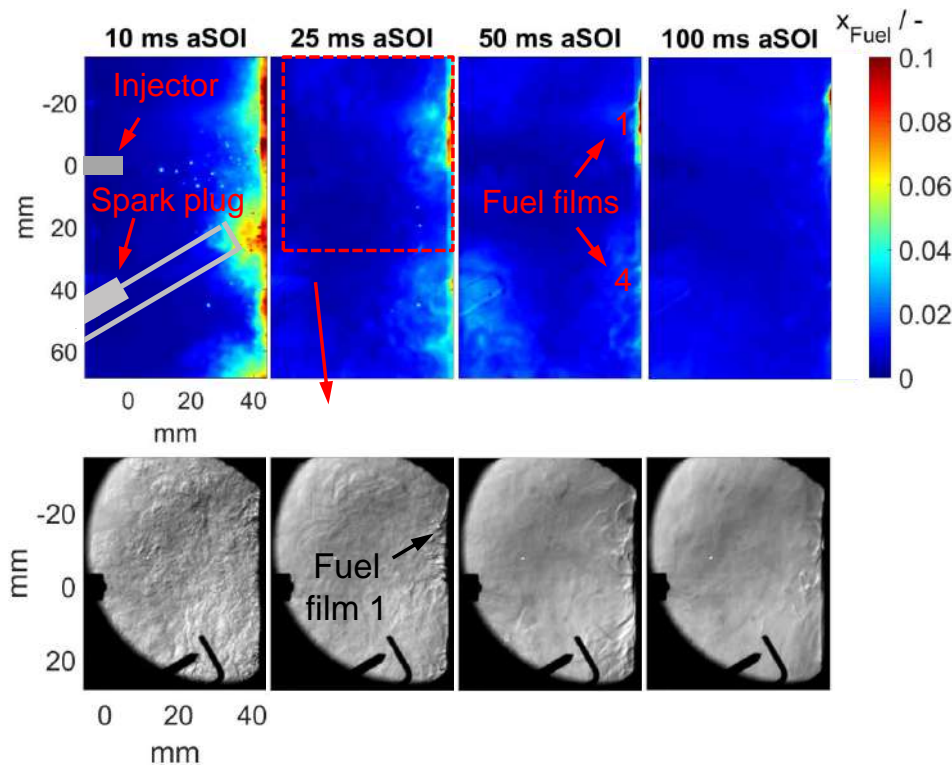

Figure 40: (top) Ensemble averages of the fuel-vapour mole-fraction and (bottom) a corresponding single sequence of schlieren images, both without combustion.

Figure 41 shows a schlieren sequence with combustion. The injection, detected by the strong extinction of light by the spray cone, hits the wall and the fuel splashes to the sides and forms film 1. A weaker intensity gradient can be seen at the edges of the spray cone, indicating the fuel's transition from liquid to vapour. At 3 ms aSOI, the injection has ended and the fuel/air mixture is ignited. Because of the bright schlieren illumination, the spark is not visible. At 7 ms aSOI the flame propagation begins in the lower right corner, where the spark has been convectively transported. The flame front is captured due to strong temperature gradients at the boundary. At 25 ms aSOI the flame has propagated through the test section. The schlieren images show strong gradients close to film 1, which correspond to density and species gradients between burnt and unburnt mixture. Additionally, natural flame luminosity, presumably soot incandescence, is superimposed on the LED light at 25 and 50 ms aSOI. Hot burnt gas from the main combustion event mixes with surrounding air and newly evaporated fuel from the liquid film, leading to the formation of a sooting flame in this region. Between 65 and 70 ms aSOI, the soot luminosity becomes stronger. Apparently, the flame is fed by fuel vapour, which emerges from the liquid film at the wall in the upper half of the image. The image at 75 ms aSOI indicates that the glowing soot is transported downstream by the flow before its luminosity cannot be seen anymore at 80 ms aSOI. The soot has either cooled down or was transported out of the field of view. Even at 100 ms aSOI, some fuel vapour still emerges from the film but soot luminosity is not visible. Most probably the gas temperature is now too low to enable pyrolytic formation of PAH.
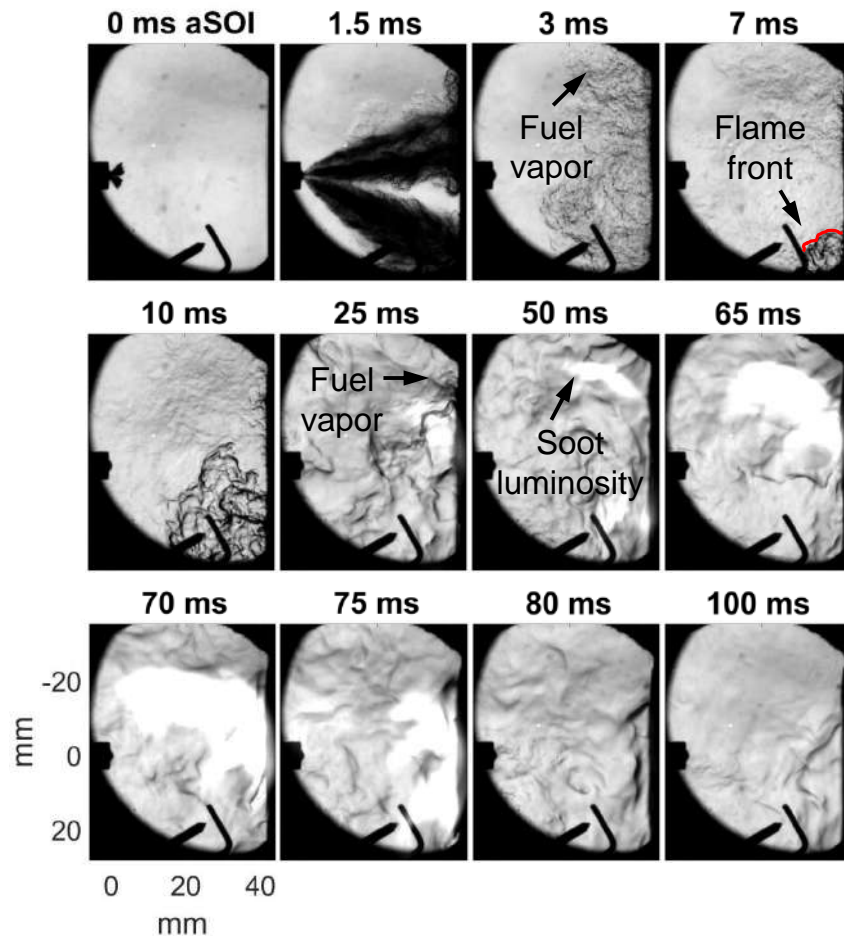
Figure 41: Schlieren images of spray, flame propagation, soot luminosity, and evaporating fuel film.

Figure 42 shows LIF images of the fuel vapour during combustion. Except for the image at 10 ms aSOI, the LIF images are ensemble averages of 10 single shots. At 10 ms aSOI, the sharply delineated low-signal region above the electrode gap corresponds to the burnt gas, in which neither fuel nor tracer are present anymore. Qualitatively, the propagation and position of the flame fronts, visualized by schlieren and LIF at 10 ms aSOI, correlate reasonably well. At 25 ms aSOI the flame has propagated through the test section and again fuel-vapour is mainly detected close to the fuel films. A quantification of the fuel-vapour mole-fraction is not possible due to spatially varying temperatures and oxygen partial-pressures.
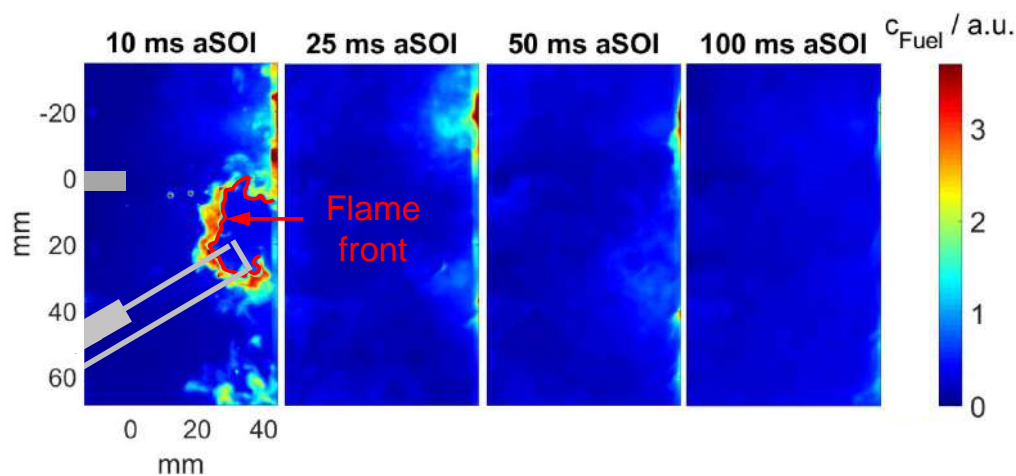

Figure 42: Ensemble averages of the relative fuel-vapour concentration in combustion.

D1.6 – Report on optical diagnostics for fuel films, mixture inhomogeneities,
soot and water injection in optical engines. Focus is on implications for models for design and control.

PaREGEn

3.3   Combustion, soot and soot precursors

Figure 43 shows single shots of PAH LIF (green) and soot LII (red), simultaneously excited according to Figure 16, in the optically accessible test section of the flow facility at different times after start of injection. Here, the injection duration was 1 ms (9.3 mg), the wall temperature was 352 K, and the flow velocity 1.8 m/s. The images are normalized to the global maxima signals of PAH LIF and soot LII within this case. This procedure is also done for the following cases. The fuel films are indicated by the purple dots on the right hand side of the images. Also the quartz wall is indicated by the grey stripe on the right. The images show that PAH and soot form in spatially well separated regions from each other. Both are detected in a shape of sharp filaments while the region of PAH appears more blurred than the one of soot. Note that the detected LIF signal, excited at 532 nm, mainly stems from large PAH with five or more aromatic rings [24].
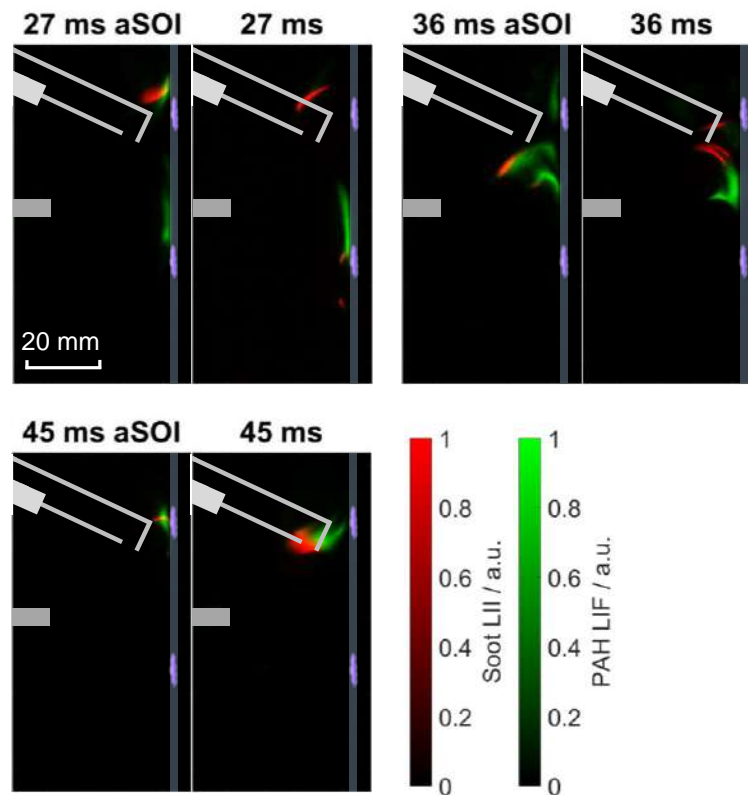

Figure 43: Single shots of PAH LIF and soot LII images for the reference case from individual combustion events.

At 27 ms aSOI, soot is detected around the spark electrodes which stems from both the evaporating fuel film in the top and liquid fuel that adheres to the spark electrodes. Slightly above the fuel film in the bottom, PAH are detected close to the wall while no soot is adjacent. At 36 ms aSOI, soot and PAH are detected in adjacent curved regions, which clearly show the transition from PAH to soot within the flow. In the first single shot, a slight overlap of the two signal regions is present. In the second image, a dark region appears between the two species, indicating the nucleation zone. Also, at that time aSOI the sooting region from above and the PAH region from below seem to merge together between the two fuel films. At 45 ms aSOI, PAH and soot mostly form in the top near film 2. Corresponding to that, Figure 44 shows a sequence of a single combustion event in the same field of view, captured with a high-speed colour camera according to Figure 15, at different times aSOI. The images are normalized to the sensor read-out, 4095 counts. The Mie scattered light of the LED visualizes the penetration of the spray through the test section right at the end of injection at 1 ms aSOI. It also indicates where the fuel impinges on the wall and forms the liquid films. At about 1.7 ms aSOI the spark ignites the fuel/air-mixture and the turbulent flame front begins to propagate through the test section as indicated by the chemiluminescence signal at 5 ms aSOI. The turbulent flame front has completely propagated through the test section at 12 ms aSOI. A first soot pocket is detected at 9 and 12 ms aSOI slightly

below film 2. This soot most presumably results from inhomogeneities forming around both the wetted spark electrodes and film 2 on the quartz wall. The soot luminosity becomes most intense at 18 ms aSOI and extinguishes with further progress in time while at the same time soot inception starts in the vicinity of film 5 in the bottom. It needs to be taken into account that, in contrast to the laser-based measurements, the signal is integrated along the line of sight so that it also contains contributions from films 1 and 4.
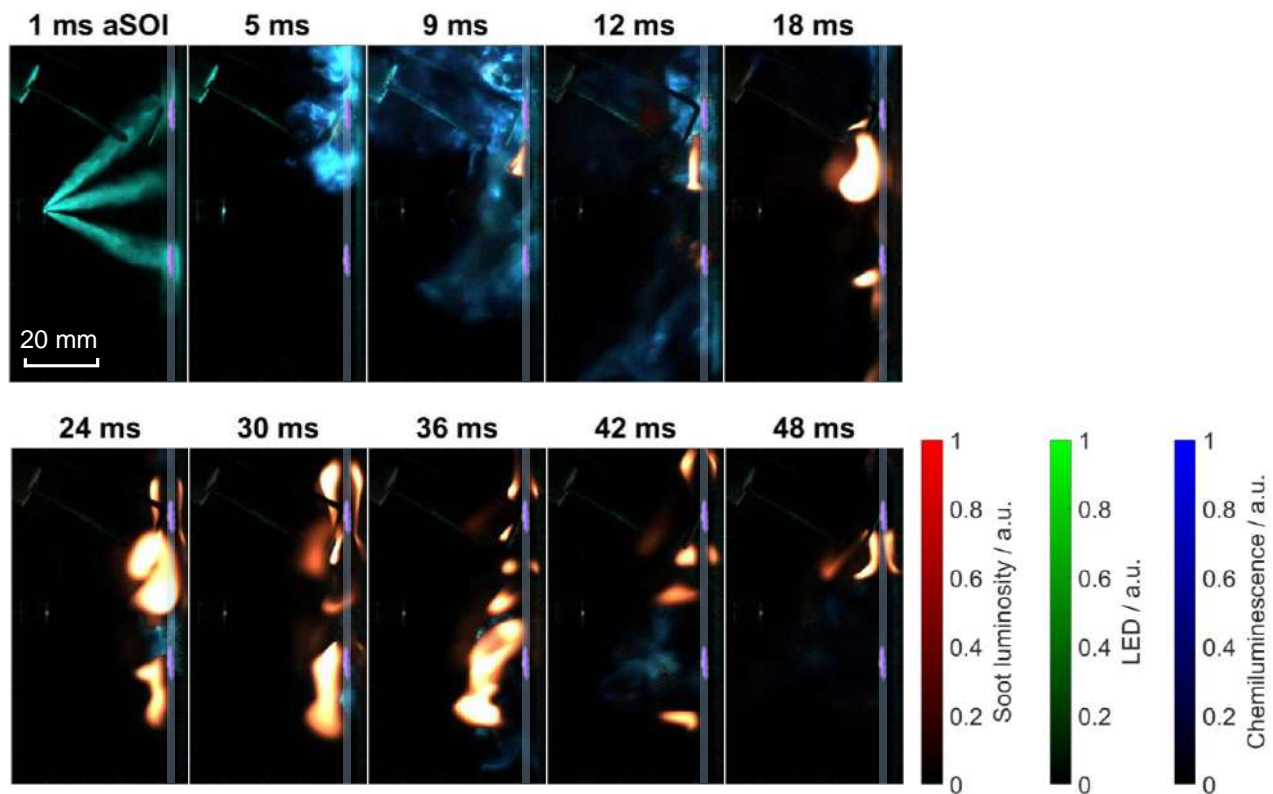

Figure 44: Sequence of high-speed images of natural soot luminosity, Mie scattered LED light from the spray, and chemiluminescence of the flame front.

Ensemble averages of 50 single shots of PAH LIF and soot LII are shown in Figure 45. Soot is detected first at 17 ms aSOI around the spark electrodes. According to the single shots, this soot most likely stems from fuel inhomogeneities around the wetted spark plug. Soot formation increases at 21 ms aSOI. No PAH are detected at that times. This might be due to the fact that the transition to soot occurs fast. At 24 ms aSOI strong PAH LIF signal is detected in the bottom of the test section, near film 5. Here, very few soot is detected near this PAH cloud. The PAH LIF signal spreads around a larger region at 27 ms aSOI. Again, soot is detected in the top of the test section near film 2 while also weak PAH LIF signal arises. At 33 ms aSOI, the two regions merge together between the two fuel films, due to the flow properties, and both PAH and soot are detected in very close vicinity and high quantities. Both signals become weaker with further progress in time. At 51 ms aSOI, no soot is detected anymore. This is either because both species are transported out of the test section or light-sheet plane or they are getting oxidized. At 51 ms aSOI, PAH LIF is detected near film 2.
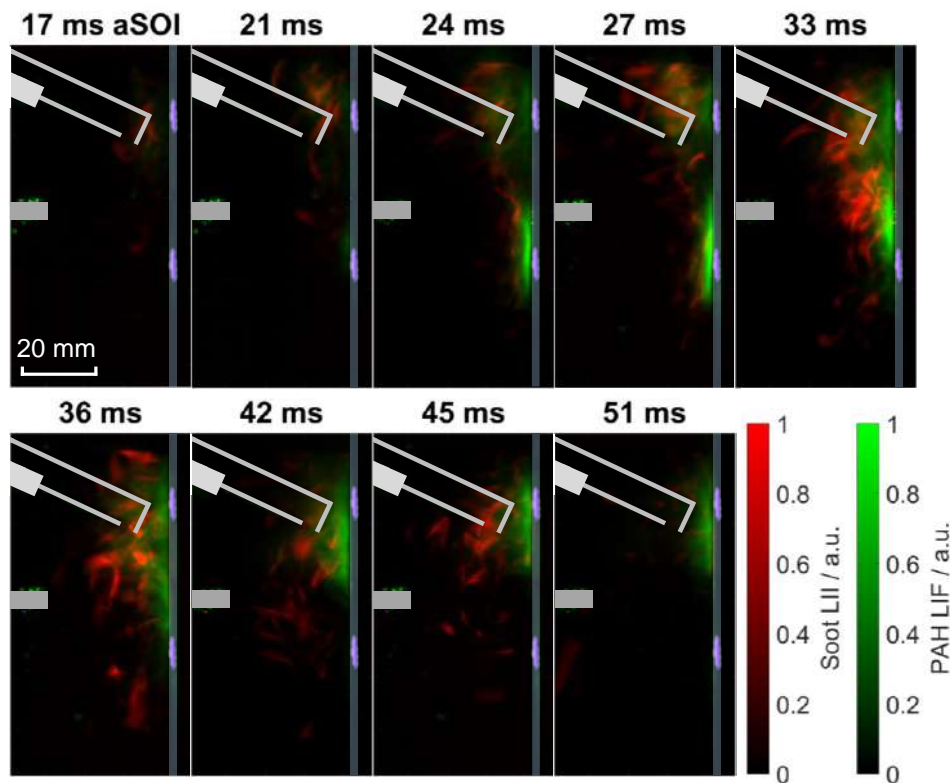
Figure 45: Ensemble average images of 50 single shots of PAH LIF and soot LII.

Ensemble averages of high-speed single shots, shown in Figure 46, visualize the flame front, indicated in blue, and soot, indicated in red. The flame front has propagated along the test section at around 12 ms aSOI, indicated by the chemiluminescence signal. Consistent with the results from Figure 45, first soot luminosity is detected in the top region, near film 2, at 15 ms aSOI. In contrast to Figure 46, significant soot is also found in the bottom near film 5 at 18 ms aSOI. At the same time, the soot luminosity around film 2 also becomes more intense. The maximum soot luminosity is detected, in good agreement with results from soot LII, at 33 ms aSOI. Chemiluminescence signal, indicating the oxidation of either fuel, PAH, or soot, is found near film 5 throughout the images in Figure 46. In a very near region, slightly upstream, strong PAH LIF signal arises between 24 and 33 ms aSOI. The correlation that PAH form in a premixed region of fuel and air, indicated by the chemiluminescence signal, was also documented by Hayashi et al. [35]. In good agreement with the visualization of PAH LIF and soot LII, the premixed region and the sooting region merge together between films 2 and 5 at 42 ms aSOI. Again, chemiluminescence is found downstream of the soot cloud, indicating the oxidation of soot and PAH transported downstream. With further progress in time, soot luminosity further diminishes and the chemiluminescence increases, indicating the oxidation of soot transported downstream. According to Figures 45 and 46, very little soot leaves the test section since even at 51 ms aSOI no LII signal is detected in the test section.
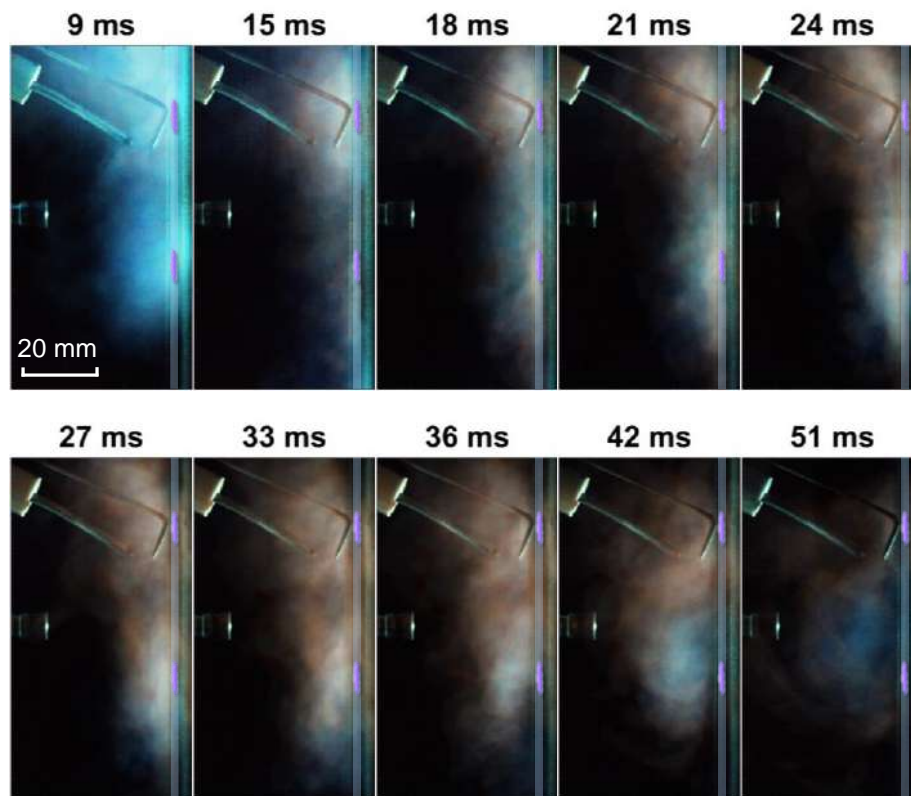
D1.6 – Report on optical diagnostics for fuel films, mixture inhomogeneities, soot and water injection in optical engines. Focus is on implications for models for design and control.

PaREGEn

Figure 46: Ensemble average images of natural soot luminosity and chemiluminescence of the flame front.

When decreasing the injection mass from 10 to 5 mg, soot is exclusively detected in the top region of the test section, as shown in the ensemble average images of PAH LIF and soot LII of 50 single shots in Figure 48. This soot results from wetting of the spark electrodes and seems to form very fast. Here, almost no PAH are detected. Early soot formation occurs around the spark electrodes at 18 ms aSOI and ends at around 36 ms aSOI. Two reasons explain the lack of soot formation from evaporating fuel films. First, the initial mass of film 5 is, according to Figure 34, about 60% lower than for the reference case with an injection mass of 9.3 mg, leading to a leaner fuel/air-mixture. Second, the total heat release is lower, coming along with lower gas temperatures, inhibiting soot formation.
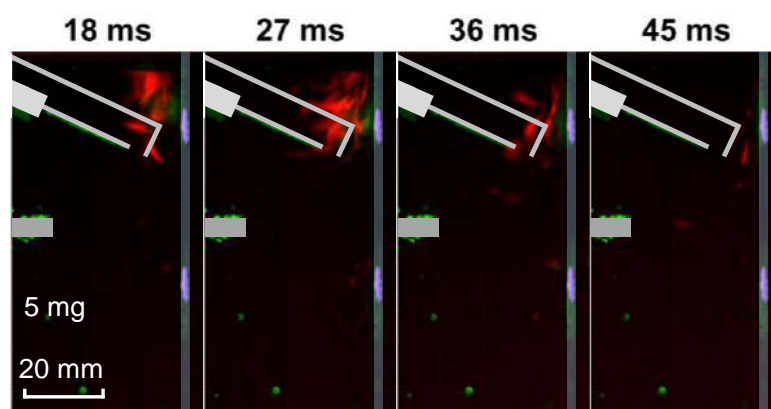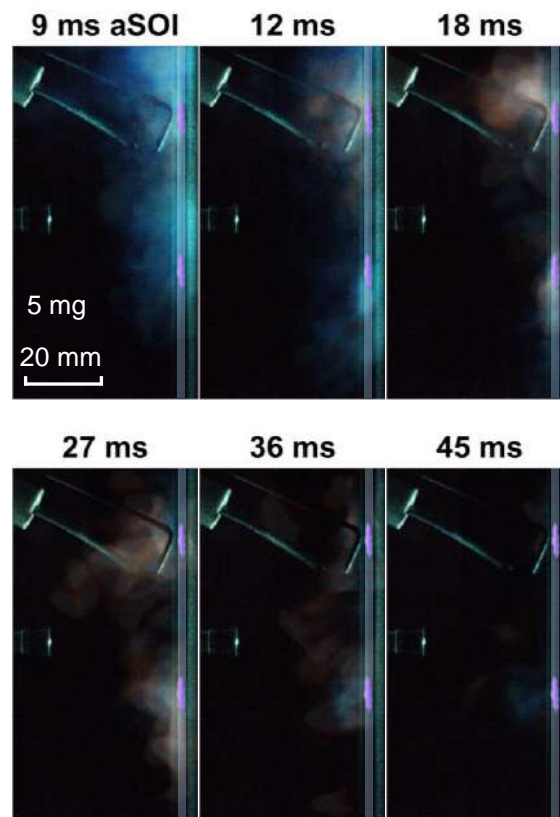

Figure 47: Ensemble average images of single shots of PAH LIF and soot LII images for an injection mass of 5 mg.

The corresponding ensemble average images of single shots of the natural flame luminosity are shown in Figure 48. Comparing the intensity and the propagation of the flame front at 9 ms aSOI with the corresponding image in Figure 46, implies the lower total heat release and incomplete combustion of the mixture. Consistent with the results from Figure 47, soot is detected around the spark electrodes from 18 to 36 ms aSOI. In contrast to the laser-based measurement, the line-of-sight images show significant soot

D1.6 – Report on optical diagnostics for fuel films, mixture inhomogeneities,
soot and water injection in optical engines. Focus is on implications for models for design and control.

PaREGEn

luminosity near fuel film 5. Also, little chemiluminescence signal is found in that area throughout the images, indicating the oxidation of soot and soot precursors.

Figure 48: Ensemble average images of natural soot luminosity and chemiluminescence of the flame front for an injection mass of 5 mg.

Images of PAH LIF and soot LII for a wall temperature of 342 K are shown in Figure 49. It needs to be taken into account that the absolute LII and LIF intensities are on average lower than for the reference case. Fuel-film masses increase when the wall temperature decreases, as shown in Figure 37. The images visualize a strong and sudden formation of PAH near film 5 at 27 ms aSOI with minor soot adjacent. Corresponding images of the natural flame luminosity are shown in Figure 50. The chemiluminescence signal indicates the oxidation of either soot or precursors or both. This might explain the incomplete formation of soot near film 5, indicated by the high PAH LIF signal. Also, the extent of the flame front is less than in the reference case, Figure 46, and ends slightly below film 5. Surprisingly, Figure 50 shows soot luminosity downstream of film 5, indicating soot that is not oxidized and leaves the test section. The resulting lower gas temperatures also inhibit soot formation. At 36 ms aSOI, again the two regions merge together and as in the reference case both PAH and soot are detected in very close vicinity. At 45 ms aSOI, soot and PAH exclusively form near film 2 in the top of the test section. The corresponding ensemble averages of the high-speed images visualize soot in similar regions at the same times and chemiluminescence downstream of the soot cloud.
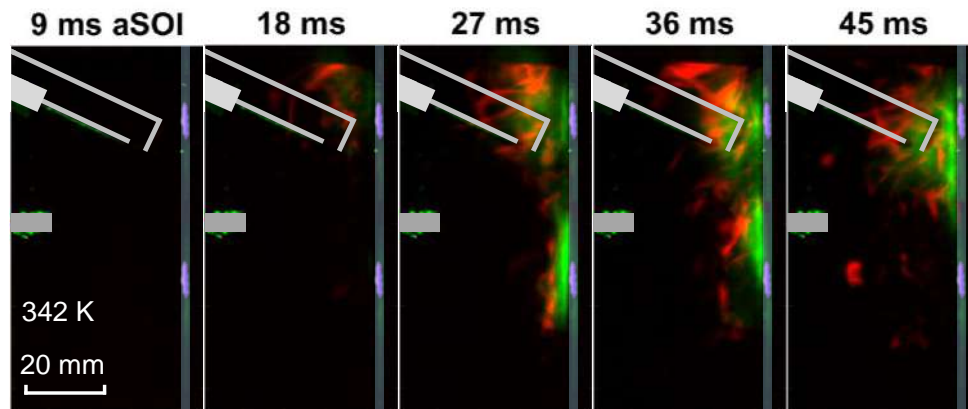
D1.6 – Report on optical diagnostics for fuel films, mixture inhomogeneities,
soot and water injection in optical engines. Focus is on implications for models for design and control.

PaREGEn

Figure 49: Ensemble average images of single shots of PAH LIF and soot LII images for a wall temperature of 342 K.
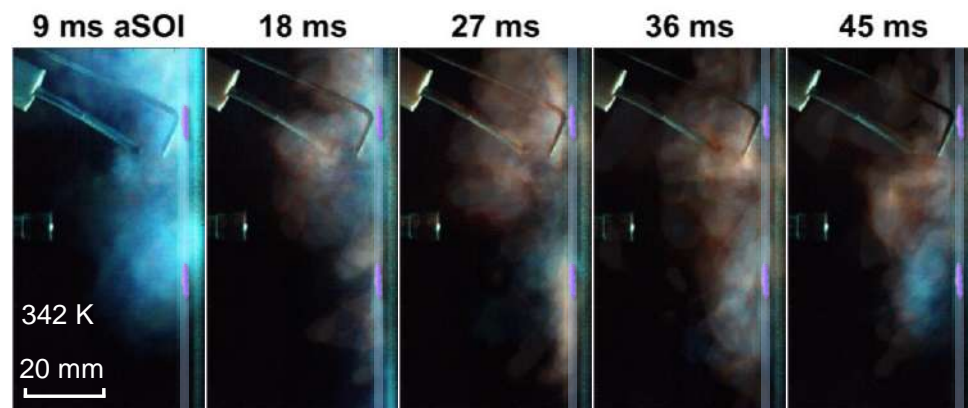

Figure 50: Ensemble average images of natural soot luminosity and chemiluminescence of the flame front for a wall temperature of 342 K.

The development of PAH and soot for an even lower wall temperature of 332 K is shown in Figure 51. Both species are mostly detected near film 2 in the top of the test section. The chemiluminescence of the flame front, shown in Figure 52, is spread over a region of lesser extent in the bottom compared to the temperature of 342 K. This indicates lower gas temperatures and prevents the formation of soot or PAH.
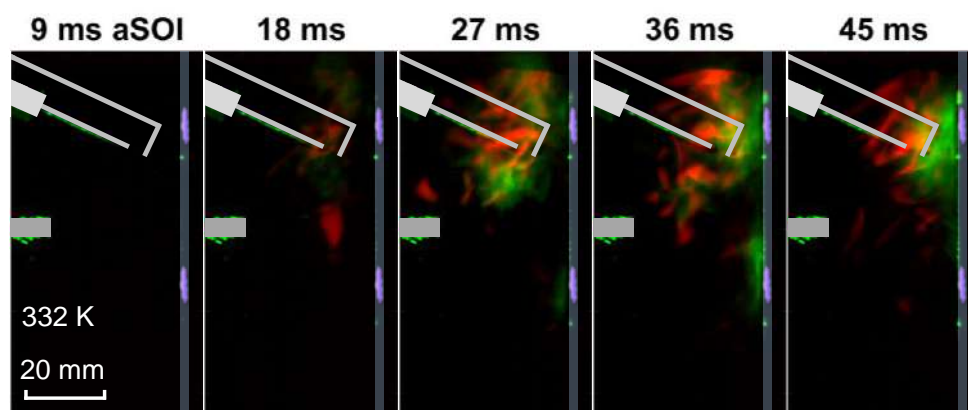

Figure 51: Ensemble average images of single shots of PAH LIF and soot LII for a wall temperature of 332 K.

The high-speed images of the natural flame luminosity show soot luminosity around the spark electrodes and near film 2 from 27 to 45 ms aSOI. Chemiluminescence is detected very close to the wall and film 2. At 45 ms aSOI the region of soot concentrates between films 2 and 5, enclosed by chemiluminescence regions in the top and in the bottom.
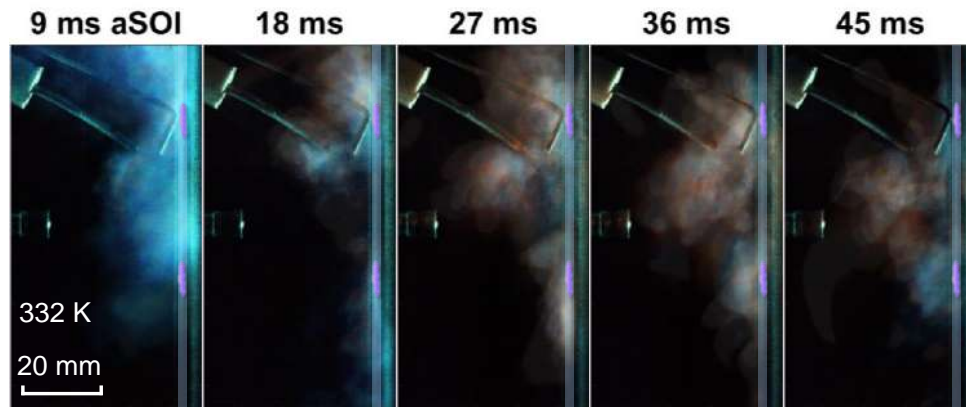
D1.6 – Report on optical diagnostics for fuel films, mixture inhomogeneities,
soot and water injection in optical engines. Focus is on implications for models for design and control.

PaREGEn

Figure 52: Ensemble average images of natural soot luminosity and chemiluminescence of the flame front for a wall temperature of 332 K.

Results for an increased flow velocity within the test section are shown in Figures 53 and 54. Here the region where PAH form in the bottom near film 5 and the region where soot forms near film 2 in the top merge together at earlier times aSOI compared to the previous cases. The chemiluminescence signal at 45 ms aSOI is stronger than in the reference case, indicating an enhanced mixing of soot precursors and soot with incoming air.
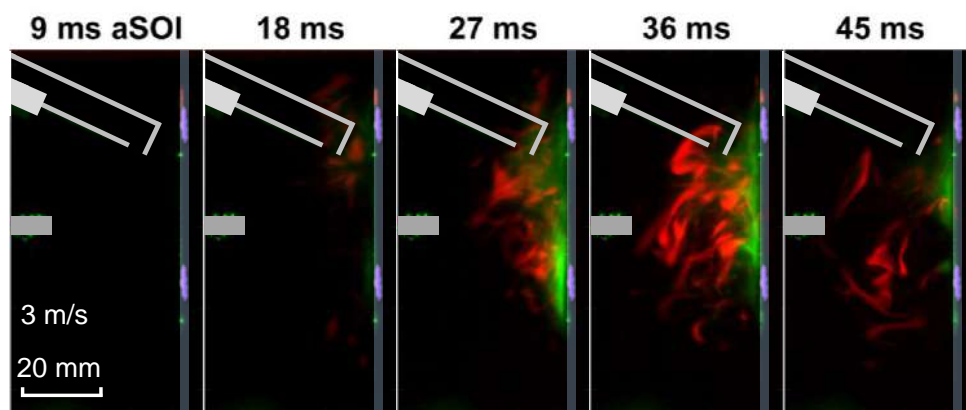

Figure 53: Ensemble average images of single shots of PAH LIF and soot LII images for a flow velocity of 3 m/s.
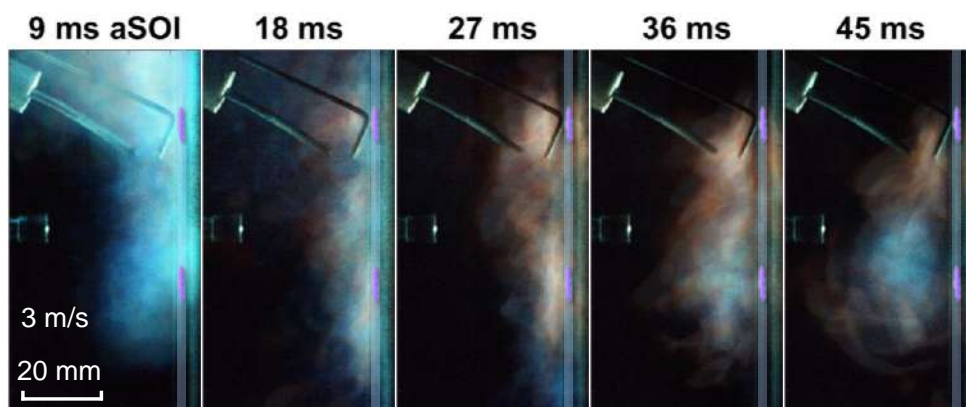

Figure 54: Ensemble average images of natural soot luminosity and chemiluminescence of the flame front for a flow velocity of 3 m/s.

Figure 55 shows single shots of a high-speed sequence for a flow velocity of 3 m/s. This sequence exemplarily visualizes the flow within the test section by showing the motion of the soot ligaments. Also here, the soot close to the spark electrodes is transported downstream while soot close to film 5 is moving upstream.
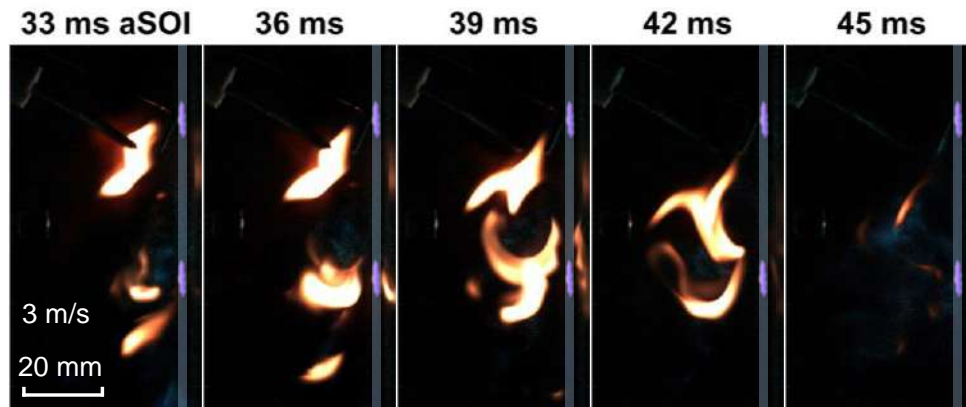
D1.6 – Report on optical diagnostics for fuel films, mixture inhomogeneities,
soot and water injection in optical engines. Focus is on implications for models for design and control.

PaREGEn

Figure 55: Single shots of a high-speed sequence of natural soot luminosity and chemiluminescence of the flame front for a flow velocity of 3 m/s.

Data of the soot volume fraction is required to develop more precise soot formation models. In addition to that the information on the presence of PAH, as a soot precursor, is also necessary. Figure 56 images the soot volume fraction at 36 ms aSOI in a single shot (left) and an ensemble average of 50 single shots (right). The LII signal was calibrated versus the soot volume fraction by an extinction measurement in the laminar diffusion flame of the Santoro burner.
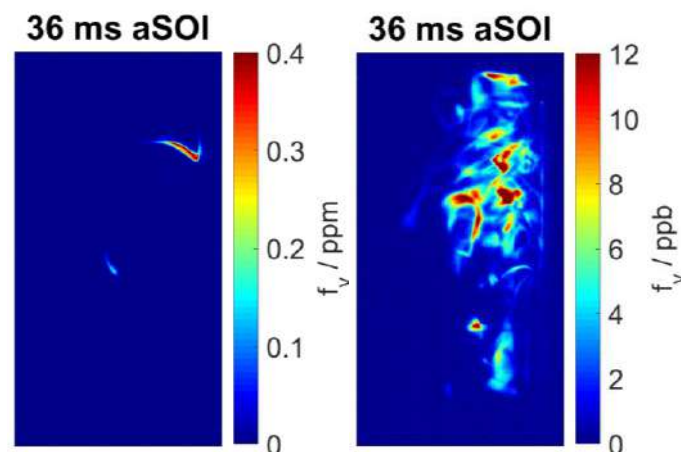

Figure 56: (left) Single shot of the soot volume fraction, (right) ensemble average image of the soot volume fraction.

D1.6 – Report on optical diagnostics for fuel films, mixture inhomogeneities, soot and water injection in optical engines. Focus is on implications for models for design and control.

PaREGEn

4 Conclusions and future work

4.1 Summary

Multiple optical imaging diagnostics were used to investigate the formation of soot from evaporating fuel films in a direct-injection model experiment. The experiment is in the optically accessible test section of a wind tunnel. A GDI injector sprays fuel into the test section. The spray evaporates and mixes with hot air at a backpressure of 1 bar, flowing from top to bottom through the tunnel. Some of the fuel impinges on the quartz wall on the opposite side of the injector and forms fuel films. A pair of electrodes ignites the fuel/air mixture. The flame front propagates through the test section and ignites sooting flames near evaporating fuel films.

The thickness of the fuel films was determined from quantitative tracer LIF imaging. The images show that the films tend to form thick droplets while evaporating from the hot quartz wall. This leads to high spatial intermittency within the fuel-film structure. Also, thin regions with thicknesses between 2 and 4 µm around the fuel film evaporate first, resulting in a high evaporation rate shortly after the end of injection and a quick decrease in the fuel film's area. Somewhat surprisingly, the results show that the evaporation rate is not influenced by whether the films evaporate in a combusting environment or not for an injection duration of 0.5 ms (5 mg). This implies that in our model experiment the convective heat transfer from the gas phase is negligible compared to the heat flux from the wall. The situation changes when the injected mass is increased to 10 mg, where the evaporation is enhanced at late times aSOI. In a real engine the air flow velocity is expected to be higher throughout the evaporation of the liquid fuel film, enhancing the convective heat transfer. A gas velocity of about 10 m/s increases the convective heat flux about a factor of five compared to the 1.8 m/s in our experiment. However, preliminary results from a model being currently developed show that the conductive heat flux from the wall is about 200 times higher than the convective one. If convective heat transfer were increased by a factor of 10, conductive heat flux from the wall would still be an order of magnitude greater.

A change in the injected affects both the fuel-film area and the fuel-film thickness. Varying the impingement distance or angle does not influence the wetted area, but the mean film thickness. Therefore, fuel film 2 with a greater impingement distance and smaller impingement angle than fuel film 5 has a similar initial area but 30% lower thickness. In a variation of the wall temperature the evaporation rate shortly after end of injection was not affected by the wall temperature. In this interval, the mass transfer of fuel from the liquid film into the gas phase appears to be governed by the highly turbulent flow near the films. After that, the evaporation rate is approximately constant and depends on the wall temperature, which also determines the film temperature and hence the vapour pressure. In a real DISI engine, fuel films evaporate from a metal surface (steel or aluminium). The heat capacity of quartz is about 1.5 times higher than the one of steel. This leads to a stronger temperature decrease of the steel in the thermal boundary layer during evaporation. However, at the same time the thermal conductivity of steel is about 30 times higher than that of quartz. This presumably compensates for the lower temperature gradient between the wall and the fuel film. Aluminium has higher heat capacity and thermal conductivity than quartz, promoting a greater heat flux from the wall to the liquid if the evaporation rate is not limited by the convective mass transport of fuel from the liquid film into the bulk gas.

In a second part of this work the mixing of the gaseous fuel from the films with air is investigated by imaging the fuel-vapour mole-fraction. The images show a high concentration of fuel-vapour near the liquid fuel films. Evaporation of fuel into the light-sheet plane is detected until 100 ms aSOI for film 1 and until 75 ms aSOI for film 4. During combustion, schlieren and LIF images both visualize the propagation of the turbulent flame front through the test section, originating from a region close to the electrodes at 10 ms aSOI. At 25 ms aSOI, natural soot luminosity is detected in the schlieren images first near the evaporating film 1. This sooting flame grows up to 70 ms aSOI. The flame extinguishes 75 ms aSOI, even though evaporation from film 1 is still

detected. Soot formation stops most probably because the gas phase temperature is too low to enable pyrolytic formation of PAH.

The third part of this work investigates the formation of soot near the evaporating fuel films by means of PAH LIF, soot LII and high-speed imaging. Preliminary in-situ measurements were done in the laminar diffusion flame of a Santoro burner. Here, PAH LIF is detected in a hollow cone region, indicating the transition from smaller PAH into large PAH. The edges of the PAH LIF cone are covered by regions of high soot LII signal, indicating the nucleation region where soot forms from PAH. Along the center axis of the flame, the PAH LIF signal peaks at a height above burner (HAB) where the LII signal strongly increases, also indicating the transition of PAH to soot.

The results from the optically accessible test section show that soot forms first close to the spark electrodes and close to film 2 in the top. Wetting the spark plug during injection causes mixture inhomogeneities in that region which presumably contribute together with the evaporation of film 2 to the soot formation. Since the origin of the flame front lies in this region and chemiluminescence intensity is highest here, higher temperatures than in other regions are expected, promoting early soot formation. Simultaneous imaging of PAH LIF and soot LII and high-speed colour combustion-imaging visualize soot formation in similar regions at different times after start of injection. The chemiluminescence signal is found at late times aSOI adjacent to film 5 in the bottom. In a very similar region, a layer of PAH is found in the close vicinity of the evaporating fuel film. The formation of PAH in a premixed region, indicated by the chemiluminescence, was already documented by Hayashi *et al.* [35]. Soot forms mostly spatially separated from the PAH and with high spatial intermittency. The chemiluminescence in the bottom of the images indicates the oxidation of soot and PAH, being transported downstream.

Although some parameters are different in a real DISI engine and change during the engine cycle, most of the findings apply also to the engine. Late injection into the chamber occurs in an engine at high ambient pressure (about 10 bar), which causes shorter spray penetration, and thus less fuel film on the piston. Also, the mixing of fuel and air might be faster due to faster flow and thus higher turbulence in an engine cylinder than in our model experiment. Both the formation and oxidation of soot might occur slightly faster during the expansion stroke in an engine due to higher collision rates of soot precursors, particles and oxidizer.

4.2   Ongoing and future work

Currently, simultaneous imaging of PAH LIF, excited at 266, 355 and 532 nm, and soot LII, excited at 1064 nm, is done in an optically accessible engine at BOSCH. As complementary line-of-sight imaging, high-speed colour combustion-imaging is also done. Figure 57 shows soot LII, excited at 1064 nm, and PAH LIF, excited at 532 nm, at 40°CA ATDC, captured simultaneously in the optically accessible engine. Apparently, the 532 nm laser also excites soot LII. But also some signal is present on the piston surface in a very small region, indicated by the white line, in the right image, which is not visible in the left image. This might be attributed to LIF of large PAH (five or more aromatic rings).
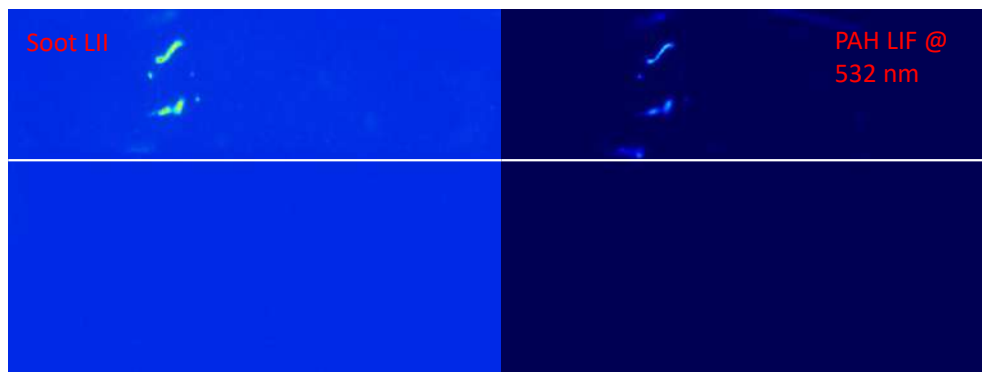
Figure 57: Single shots of (left) soot LII, excited at 1064 nm, and (right) PAH LIF, excited at 532 nm, in the optically accessible engine.

Figure 58 shows PAH LIF, excited at 355 nm, and PAH LIF, excited at 266 nm, of a different combustion event than the one shown in Figure 57. The images were simultaneously taken at 40°CA ATDC. The signals mostly lie in a similar region at the piston surface. The signal excited by 355 nm shows a higher spatial intermittency. Also further away from the piston surface and on the left side in the image @355 nm, some signal is detected where no signal is found in the right image. This signal might either be attributed to soot LII or medium size PAH (three to four rings).
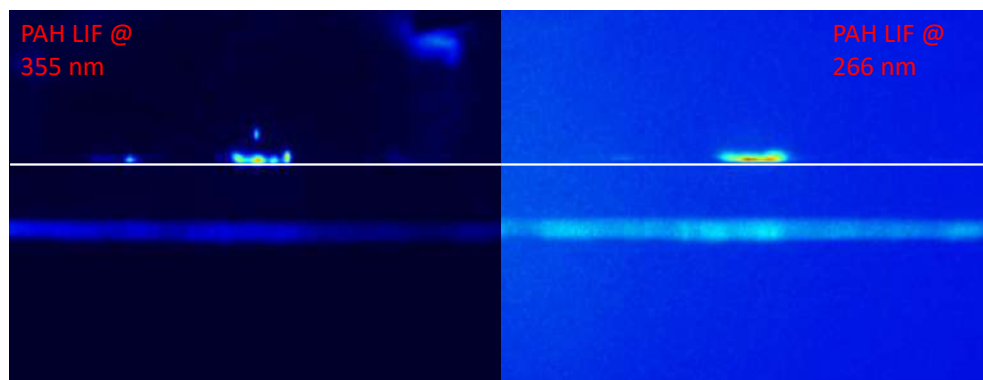

Figure 58: Single shots of (left) PAH LIF @ 355 nm and (right) PAH LIF @ 266 nm in the optically accessible engine.

To derive further conclusions from the results, captured in the optically accessible engine, intense postprocessing is required, which will be done at UDE within the next months.

The quantitative results of the fuel-film thickness, the fuel-vapour mole fraction, and the soot volume fractions currently serve as validation data for ongoing development of CFD simulations by ETH. Also, we are developing a low-dimensional model for fuel-film evaporation that should help to assess heat transfer and its impact on fuel-film evaporation and provide a better estimate of the film temperature, which is needed in the quantification of the fuel-film LIF imaging.

Fuel-vapour imaging, particle image velocimetry and PAH LIF, excited at 266 nm, will be done in the wind tunnel at UDE within the next months. In a second measurement campaign, scheduled for June/July of 2019, endoscopic imaging will be done at BOSCH. The re-scheduling of IR-absorption imaging to Q3/2019 is discussed in Section 7, Deviations and Risks.

5 References

1. Geiler, J.N., Grzeszik, R., Quaing, S., Manz, A., and Kaiser, S.A., "Development of laser-induced fluorescence to quantify in-cylinder fuel wall films," *International Journal of Engine Research* 19(33):134-147, 2018, doi:10.1177/1468087417733865.

2. Warey, A., Huang, Y., D. Matthews, R., Hall, M., and Ng, H., "Effects of Piston Wetting on Size and Mass of Particulate Matter Emissions in a DISI Engine," SAE Technical Paper 2002-01-1140, 2002, doi:10.4271/2002-01-1140.

3. Drake, M.C., Fansler, T.D., Solomon, A.S., and Szekely, G., "Piston fuel films as a source of smoke and hydrocarbon emissions from a wall-controlled spark-ignited direct-injection engine," SAE Technical Paper 2003-01-0547, 2003, doi:10.4271/2003-01-0547.

4. Ortmann, R., Arndt, S., Raimann, J., Grzeszik, R., and Würfel, G., "Methods and Analysis of Fuel Injection, Mixture Preparation and Charge Stratification in Different Direct Injected SI Engines," SAE Technical Paper 2001-01-0970, 2001, doi:10.4271/2001-01-0970.

5. Stevens, E., and Steeper, R., "Piston Wetting in an Optical DISI Engine: Fuel Films, Pool Fires, and Soot Generation," SAE Technical Paper 2001-01-1203, 2001, doi:10.4271/2001-01-1203.

6. Stojkovic, B.D., Fansler, T.D., Drake, M.C., and Sick, V., "High-speed imaging of OH* and soot temperature and concentration in a stratified-charge direct-injection gasoline engine," *Proceedings of the Combustion Institute* 30(2):2657-2665, 2005, doi:10.1016/j.proci.2004.08.021.

7. Li, J., Matthews, R.D., Stanglmaier, R.H., Roberts, C.E., and Anderson, R.W., "Further Experiments on the Effects of In-Cylinder Wall Wetting on HC Emissions from Direct Injection Gasoline Engines," SAE Technical Paper 1999-01-3661, 1999, doi:10.4271/1999-01-3661.

8. H. Stanglmaier, R., Li, J., and D. Matthews, R., "The Effect of In-Cylinder Wall Wetting Location on the HC Emissions from SI Engines," SAE Technical Paper 1999-01-0502, 1999, doi:10.4271/1999-01-0502.

9. Li, J., Huang, Y., Alger, T., et al., "Liquid Fuel Impingement on In-Cylinder Surfaces as a Source of Hydrocarbon Emissions From Direct Injection Gasoline Engines," *Journal of Engineering for Gas Turbines and Power* 123(3):659-668, 2001, doi:10.1115/1.1370398.

10. Alger, T., Huang, Y., Hall, M., and Matthews, R.D., "Liquid Film Evaporation Off the Piston of a Direct Injection Gasoline Engine," SAE Technical Paper 2001-01-1204, 2001, doi:10.4271/2001-01-1204.

11. Schulz, F., and Beyrau, F., "Systematic Investigation of Fuel Film Evaporation," SAE Technical Paper 2018-01-0310, 2018, doi:10.4271/2018-01-0310.

12. Maligne, D., and Bruneaux, G., "Time-Resolved Fuel Film Thickness Measurement for Direct Injection SI Engines Using Refractive Index Matching," SAE Technical Paper 2011-01-1215, 2011, doi:10.4271/2011-01-1215.

13. Schulz, C., and Sick, V., "Tracer-LIF diagnostics: quantitative measurement of fuel concentration, temperature and fuel/air ratio in practical combustion systems," *Progress in Energy and Combustion Science* 31(1):75-121, 2005, doi:10.1016/j.pecs.2004.08.002.

14. Trost, J., Zigan, L., Leipertz, A., Sahoo, D., and C Miles, P., "Characterization of four potential laser-induced fluorescence tracers for diesel engine applications," *Applied Optics* 52(33):8001-8007, 2013, doi:10.1364/AO.52.008001.

15. Faust, S., Goschütz, M., Kaiser, S., Dreier, T., and Schulz, C., "A comparison of selected organic tracers for quantitative scalar imaging in the gas phase via laser-induced fluorescence," *Applied Physics B* 117(1):183-194, 2014, doi:10.1007/s00340-014-5818-x.

16. Bockhorn, H., "Soot Formation in Combustion," (Heidelberg, Springer, 1994), doi: 10.1007/978-3-642-85167-4, ISBN: 3-540-58398-X.

17. Dec, J.E., zur Loye, A.O., and Siebers, D.L., "Soot Distribution in a D.I. Diesel Engine Using 2-D Laser-Induced Incandescence Imaging," SAE Technical Paper 910224, 1991, doi:10.4271/910224.

18. Dec, J.E.E., Christoph, "Ignition and Early Soot Formation in a DI Diesel Engine Using Multiple 2-D Imaging Diagnostics," SAE Technical Paper 950456, 1995, doi:10.4271/950456.

D1.6 – Report on optical diagnostics for fuel films, mixture inhomogeneities,
soot and water injection in optical engines. Focus is on implications for models for design and control.

PaREGEn

19. Dec, J.E., "A Conceptual Model of DI Diesel Combustion Based on Laser-Sheet Imaging," SAE Technical Paper 970873, 1997, doi:10.4271/970873.

20. de Francqueville, L., Bruneaux, G., and Thirouard, B., "Soot Volume Fraction Measurements in a Gasoline Direct Injection Engine by Combined Laser Induced Incandescence and Laser Extinction Method," *SAE Int. J. Engines* 3(1):163-182, 2010, doi:10.4271/2010-01-0346.

21. Hertler, D., Stirn, R., Arndt, S., Grzeszik, R., and Dreizler, A., "Investigations of soot formation in an optically accessible gasoline direct injection engine by means of laser-induced incandescence (LII)," *Applied Physics B* 104(2):399-407, 2011, doi:10.1007/s00340-011-4392-8.

22. Richter, H., and Howard, J.B., "Formation of polycyclic aromatic hydrocarbons and their growth to soot—a review of chemical reaction pathways," *Progress in Energy and Combustion Science* 26(4), 2000.

23. Geigle, K.P., O'Loughlin, W., Hadef, R., and Meier, W., "Visualization of soot inception in turbulent pressurized flames by simultaneous measurement of laser-induced fluorescence of polycyclic aromatic hydrocarbons and laser-induced incandescence, and correlation to OH distributions," *Applied Physics B* 119:717-730, 2015.

24. Bejaoui, S., Mercier, X., Desgroux, P., and Therssen, E., "Laser induced fluorescence spectroscopy of aromatic species produced in atmospheric sooting flames using UV and visible excitation wavelengths," *Combustion and Flame* 161(10):2479-2491, 2014, doi:10.1016/j.combustflame.2014.03.014.

25. Desgroux, P., Mercier, X., and Thomson, K.A., "Study of the formation of soot and its precursors in flames using optical diagnostics," *Proceedings of the Combustion Institute* 34(1):1713-1738, 2013, doi:10.1016/j.proci.2012.09.004.

26. Berlman, I.B., "Handbook of Fluorescence Spectra of Aromatic Molecules, Second Edition," (New York and London, Academic Press, 1971), 113-115, ISBN: 9780323161671.

27. Liu, P., He, Z., Hou, G.-L., Guan, B., Lin, H., and Huang, Z., "The Diagnostics of Laser-Induced Fluorescence (LIF) Spectra of PAHs in Flame with TD-DFT: Special Focus on Five-Membered Ring," *The Journal of Physical Chemistry A* 119(52):13009-13017, 2015, doi:10.1021/acs.jpca.5b10114.

28. Schoemaecker Moreau, C., Therssen, E., Mercier, X., Pauwels, J.F., and Desgroux, P., "Two-color laser-induced incandescence and cavity ring-down spectroscopy for sensitive and quantitative imaging of soot and PAHs in flames," *Applied Physics B* 78(3):485-492, 2004.

29. Lemaire, R., Faccinetto, A., Therssen, E., Ziskind, M., Focsa, C., and Desgroux, P., "Experimental comparison of soot formation in turbulent flames of Diesel and surrogate Diesel fuels," *Proceedings of the Combustion Institute* 32(1):737-744, 2009, doi:10.1016/j.proci.2008.05.019.

30. Hayashida, K., Amagai, K., Satoh, K., and Arai, M., "Experimental Analysis of Soot Formation in Sooting Diffusion Flame by Using Laser-Induced Emissions," *Journal of Engineering for Gas Turbines and Power* 128(2):241-246, 2005, doi:10.1115/1.2056536.

31. Vander Wal, R.L., Jensen, K.A., and Choi, M.Y., "Simultaneous laser-induced emission of soot and polycyclic aromatic hydrocarbons within a gas-jet diffusion flame," *Combustion and Flame* 109(3):399-414, 1997, doi:10.1016/S0010-2180(96)00189-7.

32. Leermakers, C.A.J., and Musculus, M.P.B., "In-cylinder soot precursor growth in a low-temperature combustion diesel engine: Laser-induced fluorescence of polycyclic aromatic hydrocarbons," *Proceedings of the Combustion Institute* 35(3):3079-3086, 2015, doi:10.1016/j.proci.2014.06.101.

33. Smyth, K.C., Shaddix, C.R., and Everest, D.A., "Aspects of soot dynamics as revealed by measurements of broadband fluorescence and flame luminosity in flickering diffusion flames," *Combustion and Flame* 111(3):185-207, 1997, doi:10.1016/S0010-2180(97)00017-5.

34. de Andrade Oliveira, M.H., Olofsson, N.E., Johnsson, J., et al., "Soot, PAH and OH measurements in vaporized liquid fuel flames," *Fuel* 112:145-152, 2013, doi:10.1016/j.fuel.2013.05.006.

35. Hayashi, J., Hashimoto, N., Nakatsuka, N., et al., "Simultaneous imaging of Mie scattering, PAHs laser induced fluorescence and soot laser induced incandescence to a lab-scale turbulent jet pulverized coal flame," *Proceedings of the Combustion Institute* 37(3):3045-3052, 2019, doi:10.1016/j.proci.2018.09.028.

36. Raza, M., Chen, L., Leach, F., and Ding, S., "A Review of Particulate Number (PN) Emissions from Gasoline Direct Injection (GDI) Engines and Their Control Techniques," *Energies* 11(6), 2018, doi:10.3390/en11061417.

37. Robinson, J.W., "Atomic Spectroscopy, Second Edition," (Boca Raton, Taylor & Francis, 1996), 27-28, ISBN: 9780824797423.

38. Zhao, H., "Laser Diagnostics and Optical Measurement Techniques in Internal Combustion Engines," (Warrendale, SAE International, 2012), ISBN: 9780768057829.

39. Senda, J., Ohnishi, M., Takahashi, T., Fujimoto, H., Utsunomiya, A., and Wakatabe, M., "Measurement and Modeling on Wall Wetted Fuel Film Profile and Mixture Preparation in Intake Port of SI Engine," SAE Technical Paper 1999-01-0798, 1999, doi:10.4271/1999-01-0798.

40. Faust, S.M., "Characterisation of organic fuel tracers for laser-based quantitative diagnostics of fuel concentration, temperature, and equivalence ratio in practical combustion processes," Dissertation, Mechanical and Process Engineering Department, University of Duisburg-Essen, Duisburg, 2013.

41. Park, S., and Ghandhi, J.B., "Fuel Film Temperature and Thickness Measurements on the Piston Crown of a Direct-Injection Spark-Ignition Engine," SAE Technical Paper 2005-01-0649, 2005, doi:10.4271/2005-01-0649.

42. Koban, W., Koch, J.D., Hanson, R.K., and Schulz, C., "Oxygen quenching of toluene fluorescence at elevated temperatures," *Applied Physics B* 80(6):777-784, 2005, doi:10.1007/s00340-005-1769-6.

43. Benzler, T., Endres, T., Dreier, T., and Schulz, C., "Temperature, pressure, and oxygen quenching behavior of fluorescence spectra and lifetimes of gas-phase o-xylene and 1,2,4-trimethylbenzene," *Applied Physics B* 124(4):70, 2018, doi:10.1007/s00340-018-6937-6.

44. Michelsen, H.A., Schulz, C., Smallwood, G.J., and Will, S., "Laser-induced incandescence: Particulate diagnostics for combustion, atmospheric, and industrial applications," *Progress in Energy and Combustion Science* 51:2-48, 2015, doi:10.1016/j.pecs.2015.07.001.

45. Santoro, R.J., Semerjian, H.G., and Dobbins, R.A., "Soot particle measurements in diffusion flames," *Combustion and Flame* 51:203-218, 1983, doi:10.1016/0010-2180(83)90099-8.

46. Desgroux, P., Mercier, X., Lefort, B., Lemaire, R., Therssen, E., and Pauwels, J.F., "Soot volume fraction measurement in low-pressure methane flames by combining laser-induced incandescence and cavity ring-down spectroscopy: Effect of pressure on soot formation," *Combustion and Flame* 155(1):289-301, 2008, doi:10.1016/j.combustflame.2008.05.016.

47. Bladh, H., and Bengtsson, P.E., "Characteristics of laser-induced incandescence from soot in studies of a time-dependent heat- and mass-transfer model," *Applied Physics B* 78(2):241-248, 2004, doi:10.1007/s00340-003-1362-9.

48. Zheng, Y., Xie, X., Lai, M.-C., and VanDerWege, B. "Measurement and Simulation of DI Spray Impingements and Film Characteristics," presented at ICLASS 2012, Germany, September 2-6, 2012.

49. Schulz, F., Samenfink, W., Schmidt, J., and Beyrau, F., "Systematic LIF fuel wall film investigation," *Fuel* 172:284-292, 2016, doi:10.1016/j.fuel.2016.01.017.

50. Schulz, F., Schmidt, J., and Beyrau, F., "Development of a sensitive experimental set-up for LIF fuel wall film measurements in a pressure vessel," *Experiments in Fluids* 56(5), 2015, doi:10.1007/s00348-015-1971-1.

51. Cheng, Y.-s., Deng, K., and Li, T., "Measurement and simulation of wall-wetted fuel film thickness," *International Journal of Thermal Sciences* 49(4):733-739, 2010, doi:10.1016/j.ijthermalsci.2009.10.006.

52. Jüngst, N., and Kaiser, S., "Imaging of Fuel-Film Evaporation and Combustion in a Direct-Injection Model Experiment," SAE Technical Paper 2019-01-0293, 2019, doi:10.4271/2019-01-0293.

6 Deviations and Risks

6.1 Deviations

In Subtask 1.3.2, IR absorption imaging is to be used in the optical single cylinder engine for measurements of in-cylinder water distribution and wall-films. This Subtask was not finished as planned in the period covered by this report. Instead, priority was given to the more complex than anticipated development of the diagnostics for fuel films, soot, and soot precursors (described in Sections 2 and 3), because the knowledge gap in the area of in-cylinder soot formation from fuel films was considered more important.

Experiments on IR imaging first in the (simpler) flow channel at the IVG and then in the (more complex) optical engine at BOSCH are planned for Q3 2019.

6.2 Risk Register

Risk No.	What is the risk?	Probability of risk occurrence[3]	Effect of risk[4]	Solutions to overcome the risk
1	Section 3.1: Accuracy in the predicted fuel-film thicknesses and evaporation rates. Error sources are known and seem to have no significant effect here.	2	1	Repetition of fuel-film imaging to check the replicability of the results
2	Section 3.3: Excitation of soot LII when exciting PAH LIF with 532 nm. Accuracy in the predicted soot volume fractions.	1	1	Reduce the laser fluence for excitation of PAH LIF to a minimum so that no soot LII is excited.
3	Section 4: Determining the flow field in the wind tunnel with PIV during combustion => Seeding of solid particles might be problematic	2	1	Try seeding of liquid particles without combustion. If liquid particles do not propagate through sieves in the intake, remove sieves for first tests.
4	Excitation of different size PAH by exciting LIF with different wavelengths	1	2	Use of appropriate filters to differentiate between the signals
5	Pressure in flow channel is, in contrast to DI SI engine, equal to ambient pressure => might influence the combustion process and the subsequent soot formation	1	2	More focus on work in the optical engine, which operates with "real" engine pressures
6	IR-absorption imaging of water in the optical engine does not work on tight time schedule	2	1	Test the imaging method first in the flow channel, as with other diagnostics in the past

---

[3] Probability risk will occur: 1 = high, 2 = medium, 3 = Low

[4] Effect when risk occurs: 1 = high, 2 = medium, 3 = Low

Appendix A – Acknowledgement

The author(s) would like to thank the partners in the project for their valuable comments on previous drafts and for performing the review.

Project partners:

#	Partner	Partner Full Name
1	RIC	RICARDO UK LIMITED
2	DAI	DAIMLER AG
3	JLR	JAGUAR LAND ROVER LIMITED
4	BOSCH	ROBERT BOSCH GMBH
5	FEV	FEV EUROPE GMBH
6	JM	JOHNSON MATTHEY PLC
7	HON	HONEYWELL, SPOL. S.R.O
8	JRC	JOINT RESEARCH CENTRE – EUROPEAN COMMISSION
9	UNR	UNIRESEARCH BV
10	IDIADA	IDIADA AUTOMOTIVE TECHNOLOGY SA
11	SIEMENS	SIEMENS INDUSTRY SOFTWARE SAS
12	LOGE	LUND COMBUSTION ENGINEERING LOGE AB
13	ETH	EIDGENOESSISCHE TECHNISCHE HOCHSCHULE ZUERICH
14	UDE	UNIVERSITAET DUISBURG-ESSEN
15	RWTH	RWTH AACHEN UNIVERSITY
16	UFI	UFI FILTERS SPA
17	UOB	UNIVERSITY OF BRIGHTON